UNIVERSITÀ DEGLI STUDI DI PADOVA

Dipartimento di Fisica e Astronomia “Galileo Galilei”

Master Degree in Astrophysics and Cosmology

Final Dissertation

Internal Kinematics of Stellar Populations in The Globular Cluster NGC 6266

Thesis supervisor
Prof. Antonino P. Milone
Thesis co-supervisors
Tuila Ziliotto
Fabrizio Muratore

Candidate
Matteo Barbieri

Academic Year 2023/2024

Abstract

Globular clusters are mainly composed of two groups of stars known as first and second populations. The first population shows the same chemical composition as alpha-enhanced field stars from the Galactic halo, while the second population is enriched in He, N, Na, and Al, and depleted in C, O, and Mg. Several formation scenarios have been proposed to explain their origin, but none fully satisfy the observational data. According to many of these scenarios, second population stars originated from material ejected into the interstellar medium by more massive first-population stars. Other theories suggest that globular clusters consist of a single generation of stars, and the second population acquired its particular chemical composition due to exotic physical phenomena that occurred in the proto-globular cluster.

Dynamical simulations that assume multiple populations as the result of a sequence of distinct episodes of star formation predict different kinematic signatures for first and second population stars. While the observational study of the kinematic properties of these multiple populations is still in its early stages, promising results have emerged from the analysis of clusters published so far in the literature.

In this thesis, I extended these studies to the Galactic globular cluster NGC 6266. First, I performed state-of-the-art photometry to reduce observations collected by the Hubble Space Telescope at two different epochs. This approach allowed me to obtain both the photometric and astrometric catalogs for this cluster. After correcting the photometric catalog for differential reddening, I produced the first chromosome map for NGC 6266, successfully distinguishing between first and second population stars in both the red giant branch and the main sequence. Finally, I developed a Markov Chain Monte Carlo approach to estimate the intrinsic velocity dispersion of the radial and tangential components of stars in each population as a function of their distance from the cluster center.

The results of this work reveal no significant differences in the kinematic behavior of the two populations within 2.5 arcminutes from the cluster center, a region extending to twice the half-light radius of the cluster. This finding might initially appear consistent with a single-generation scenario, where minimal or no kinematic differences are expected between first- and second-population stars.

A more plausible explanation, however, lies in the dynamical evolution of the cluster. In the inner regions, two-body relaxation may have erased any initial kinematic differences between the populations. For a cluster like NGC 6266, the half-mass relaxation timescale is significant compared to its age, making this process a likely contributor to the observed uniformity. Understanding the implications of two-body relaxation is therefore essential for assessing the impact of dynamical age on the cluster's kinematics.

It is important to note that the absence of detected kinematic differences in this study does not exclude their presence at larger distances from the cluster center. Observations covering a larger field of view will be necessary to explore this possibility further and to better understand the cluster's overall dynamical state.

Contents

List of Figures

List of Tables

List of Acronyms

ACS Advanced Camera for Surveys

AGB Asymptotic Giant Branch

AGC Anomalous Globular Cluster

CCD Charge-Coupled Device

ChM Chromosome Map

CMD Color-Magnitude Diagram

DEC Declination

ePSF effective PSF

FRMS Fast Rotating Massive Star

FoV Field of View

1P First Population

GC Globular Clusters

HST Hubble Space Telescope

iPSF instrumental PSF

ISM Interstellar Medium

JWST James Webb Space Telescope

JD Julian Date

ΛCDM Lambda Cold Dark Matter

MS Main Sequence

MCMC Markov Chain Monte Carlo

MIB Massive Interacting Binaries

PSF Point Spread Function

RGB Red Giant Branch

RA Right Ascension

2P Second Population

SSP Simple Stellar Population

SMS Super Massive Star

WFC3 Wide Field Camera 3

Chapter 1

Key Observations in Globular Clusters

This chapter is dedicated to introducing globular clusters and analyzing their properties. First, I will provide a general overview of their characteristics. Then, I will explore the phenomenon of multiple populations, discussing how it was discovered and its implications.

Globular Clusters (GC) are spheroidal collections of stars that predominantly orbit in the periphery of galaxies. They range in size from 10 to 30 parsecs (pc) and can contain up to millions of stars, which are highly bound by gravity. GCs are among the oldest objects in the Universe, with astronomers estimating their formation at redshift $z \gtrsim 3$ (Dotter et al., 2009). Moreover, their stars are typically metal poor. For this reason, they are considered some of the best fossil records for studying the primordial Universe. Studying the chemical composition of these clusters provides direct insights into the primordial chemical composition of the Universe and the formation history of our Galaxy.
Their stellar populations are predominantly old, metal-poor stars. Until about 20 years ago, GCs were considered the best examples of Simple Stellar Population (SSP) in the Universe (Renzini and Buzzoni, 1986). A SSP is defined as an assembly of coeval and initially chemically homogeneous single stars. Such a population is described by four properties:

1. **Age**: All stars in the population formed at the same time.

2. **Chemical composition**: Since they originated from the same nebula, they share the same chemical composition.

3. **Initial mass function**: These stars share the same initial mass distribution, having formed from the same molecular cloud.

4. **Distance**: All stars in the population are at roughly the same distance from us, as they formed together in the same region of space.

If any of these properties are not fulfilled, the population is considered complex, meaning it is composed of several SSPs.

An important tool to study the properties of GCs is the Color-Magnitude Diagram (CMD), which is a plot where the $\hat{x}$-axis represents a color and the $\hat{y}$-axis represents a magnitude. This diagram is fundamental for studying stellar populations since stars are not randomly distributed on it but occupy precise areas depending on their specific properties.
According to simulations, the SSP nature of GCs is shown by the narrow sequence of stars in the optical CMD. This can be seen in Figure 1.1 for the case of NGC 6397.

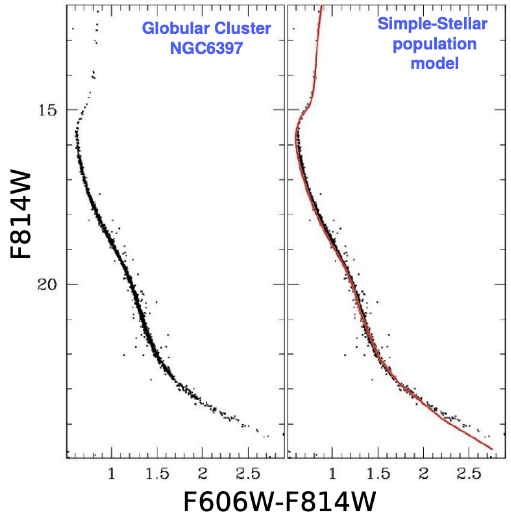

Figure 1.1: Example of the best photometry achievable in the early 2000s, applied to the study of GCs (Anderson et al., 2008). The theoretical model for a simple stellar population (the red line) perfectly matches the observational data.

Although this image represents state-of-the-art photometry and shows a perfect agreement between data and theoretical models, represented by the red isochrone in the right image, astronomers discovered hidden complexities in GCs that indicated they could no longer be considered SSPs.

Initial observations of different light element abundances in GCs stars date back to the 1980s, when several spectroscopic studies began detecting the anticorrelation of carbon and nitrogen in the red giant branch of NGC 6752 and 47 Tucanae (Norris et al., 1981; Norris and Freeman, 1982). Although these observations provided the first evidence of stars with different chemical compositions in GCs, they were limited to small samples. Therefore, these observations alone could not prove the existence of multiple populations but were sufficient to challenge the idea that GCs were simple stellar populations.

The breakthrough in our understanding came with the advent of Hubble Space Telescope (HST) photometry. Thanks to HST, which significantly improved the precision and quality of photometric observations, and the development of sophisticated analysis codes, it became possible to identify multiple sequences in the CMD. These sequences were later confirmed through spectroscopy as signatures of multiple stellar populations (see Figure 1.2).

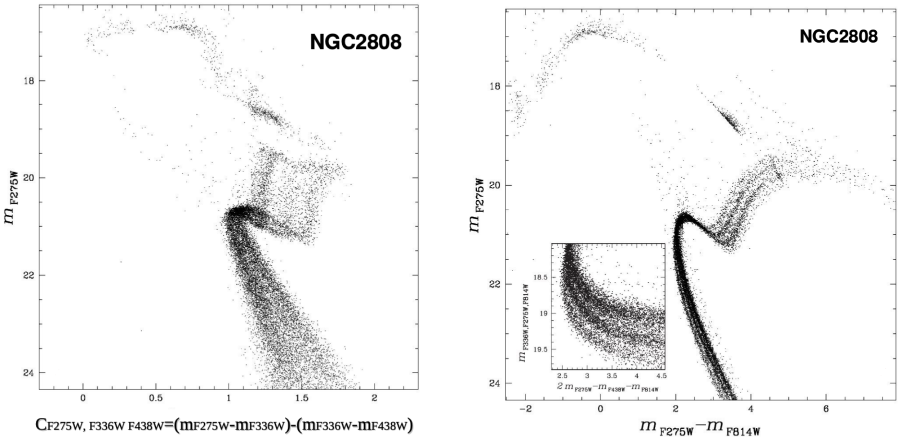

Figure 1.2: Multiple populations in NGC 2808 (Milone et al., 2015). Using appropriate filter combinations, CMDs highlight the presence of multiple sequences.

The choice of filters used to build the diagrams in Figure 1.2 was not random; they were selected to be sensitive to variations in light elements observed in spectroscopy. These chemical variations are related

to products of hot-hydrogen burning and proton-capture processes, resulting in an enhancement of He, N, Na, Al, and a depletion of C, O, and Mg (Carretta et al., 2009; Marino et al., 2019).
Among these discussions, Milone et al. (2011, 2015) introduced two new photometric tools that have become fundamental in analyzing multiple populations. The first is a new class of CMD, called **super-CMD**, where the $\hat{x}$-axis is no longer a simple color but a combination of colors (Milone et al., 2011), called pseudo-color, highlighting the chemical dependencies mentioned above.
In the left panel of Figure 1.2, the pseudo-color $C_{F275W,\,F336W,\,F438W}$ shows a splitting of the classical CMD narrow line into multiple sequences at the level of the red giant branch. Since the main sequence remains well-defined, this split cannot be attributed to differential reddening effects but is interpreted as a physical split representing the existence of multiple stellar populations.
The second tool, introduced a few years later, is known as the Chromosome Map (ChM) (Milone et al., 2015). This map is obtained by considering two different super-CMDs of the same cluster, each using different filter combinations and thus sensitive to different chemical abundances. The procedure for obtaining this map will be discussed in detail in Chapter 4, where I will present, for the first time, the ChM of the GC NGC 6266.

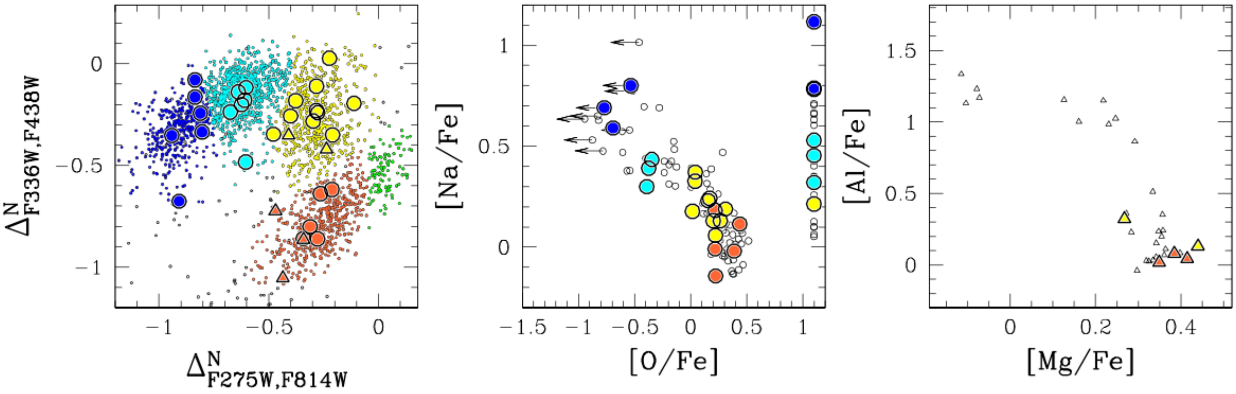

Figure 1.3: Left panel: ChM of the Galactic GC NGC 2808. Different colors identify different populations. Points marked with larger symbols indicate stars for which spectroscopic measurements are available in the literature. Central panel: Sodium-Oxygen anticorrelation for RGB stars of NGC 2808. Right panel: Magnesium-Aluminum anticorrelation for RGB stars of NGC 2808 (Milone et al., 2015).

The ChM, shown in the first panel of Figure 1.3, is essentially a two-color diagram where the quantities plotted on the axes are not simple colors but are colors that have been verticalized. In this way, different populations appear as blobs that can be easily recognized. In the initial work on this technique, Milone et al. (2015) compared this map with spectroscopic observations of the same sample of stars (middle and right panels of Figure 1.3), proving that these clustering properties directly reflect the chemical composition of different populations.

Based on these revolutionary studies, the phenomenon of multiple populations has become a well-studied topic in the past ten years. Moreover, extending the study to a larger sample of clusters (some of them are shown in figure 1.4) has led to identifying important properties regarding the nature of globular clusters, which will briefly discussed in the rest of the chapter.

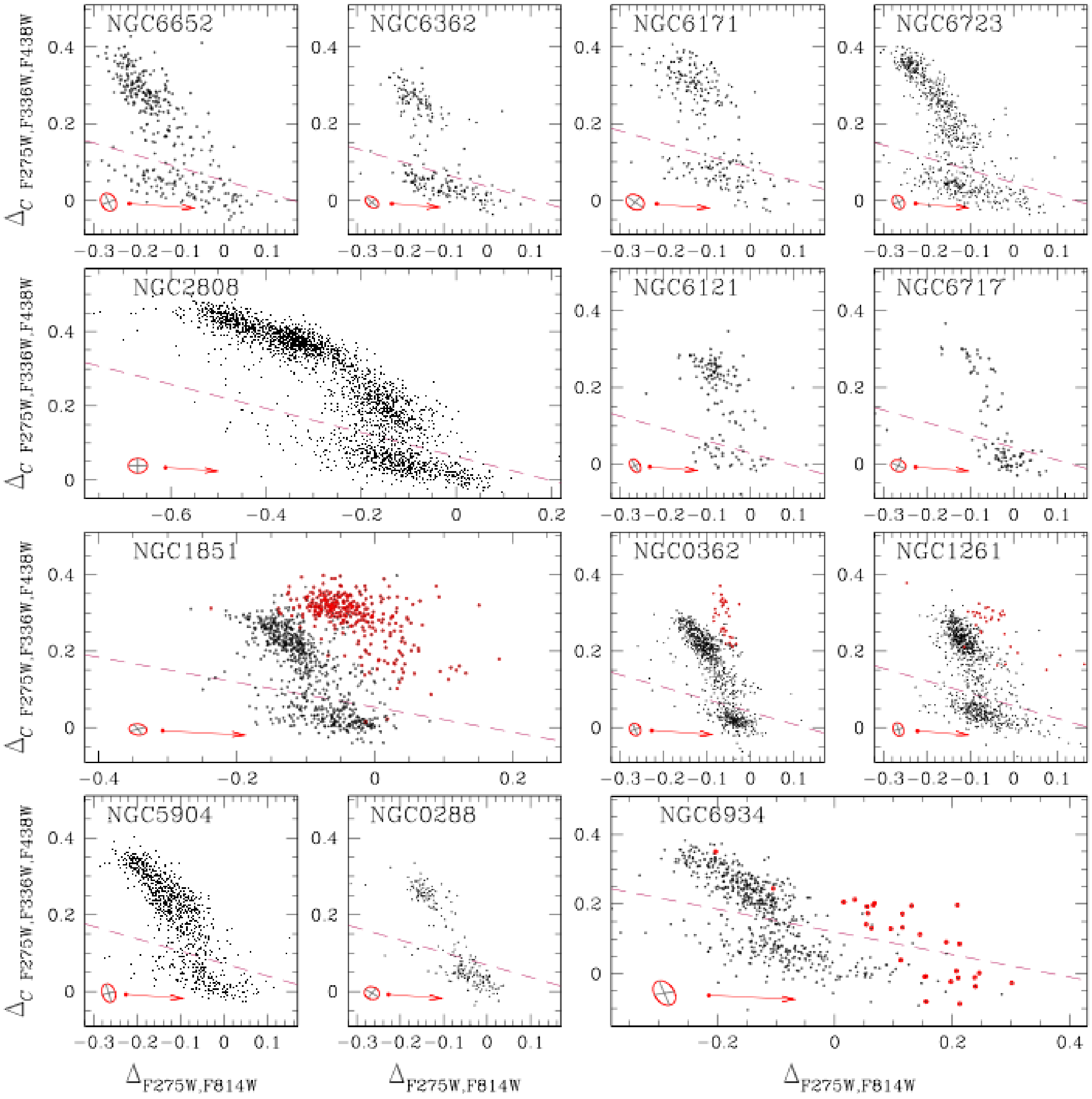

Figure 1.4: ChMs for a sample of 13 GCs, from Milone et al. (2017). ChMs with red dots indicate GCs that have been classified as anomalous.

1G-2G Discreteness

In all Galactic GCs, the presence of at least two populations of stars have been identified, known as First Population (1P) and Second Population (2P) (Milone et al., 2017; Marino et al., 2019). By examining the chromosome maps in figure 1.4, we can observe this behaviour clearly.
The lower population in each diagram represents 1P, while the upper one corresponds to 2P.
Chemically, 1P exhibits a composition similar to that of Galactic field stars, showing consistency across different clusters. In contrast, 2P displays a chemical composition, as described in the previous sections, that varies from cluster to cluster.
In the figure 1.4, the red circle represents the expected appearance of the 1P (with the arrow indicating its location on the plot) under the hypothesis of a SSP model. Additionally, we observe that the two populations are well separated; they do not form a continuous distribution but rather a **discrete** one.

Ubiquity and Variety

ChMs generated using appropriate color combinations show that multiple populations are a common phenomenon in Galactic GCs (Milone et al., 2017), demonstrating that their formation mechanism is widespread throughout the Milky Way.
However, despite the prevalence of multiple populations across Galactic GCs, each cluster exhibits its own unique characteristics, highlighting the variety within this otherwise universal phenomenon. As shown in figure 1.4, no two clusters display identical morphological properties in their ChMs. Factors such as cluster mass, age, metallicity, and dynamical history likely contribute to these variations, creating a broad spectrum of outcomes. This diversity reflects the complex and multifaceted nature of GC formation and evolution.

Two Classes: Type I and Type II GCs

Studying the ChMs in figure 1.4, it is possible to notice that GCs can be divided into two classes based on their morphological characteristics. For instance, the ChM of NGC 1851 shows the presence of an additional population of stars, represented by red dots in the figure.
Thus, we define type I GCs[1], which accounts for 82% of known GCs, as those characterized by the two-populations patter. In contrast, type II GCs[2], which represents the remaining 18% of GCs, are characterized by an additional sequence of stars, showing star-to-star variations in iron and s-elements (Marino et al., 2021).

During the '90*s* astronomers discovered that M54, which is now classified as a type II GCs, was associated with the nucleus of the Sagittarius dwarf galaxy (Ibata et al., 1994). This galaxy is interacting with the Milky Way and is expected to merge with it in a few billion years. However, the compact nuclei of dwarf galaxies can survive the merging process, making M52 the best connection we have between GCs and relic nuclei of dwarf galaxies.
Another important difference between type I and II GCs is their potential to host an intermediate mass black hole. For many years, both types were considered strong candidates for hosting such black holes, but to date, there has been no evidence of their presence in type I GCs. The recent discovery of anomalous fast rotating stars in the core of Omega Centauri, suggests the presence of an intermediate-mass black hole at the center of this cluster (Häberle et al., 2024). Omega Centauri is another example of a type II GCs, and this observation provides strong evidence that the origin of these two classes of GCs may be different.

Dependence on Cluster Mass

One hypothesis that has been tested in the past years is related to the possibility that the mass of a GCs can be a possible threshold for the presence of multiple populations.
An observation that may support this hypothesis is that comparing the lightest GCs (NGC 6535,

---

[1] Also known as normal GCs

[2] Also known as anomalous GCs.

$\log(M/M_{\odot}) = 3.4$) with the heaviest GCs (Omega Centauri, $\log(M/M_{\odot}) = 6.4$) it is possible to notice that the first one hosts only two populations, while the second one hosts 16 stellar populations (Milone et al., 2017).

More quantitatively, some observations (upper panels of figure 1.5) show that the maximum helium variation of GCs correlates with the cluster mass (Milone et al., 2018a). This is confirmed by observations demonstrating that also the width of the RGB in the pseudo-color $C_{F336W,\,F438W,\,F814W}$ (lower panel of figure 1.5) correlates with the cluster mass. This pseudo-color is sensitive to the variation nitrogen (Lagioia et al., 2019).

All these observations suggests the presence of a possible mass threshold regards the presence of multiple populations in GCs.

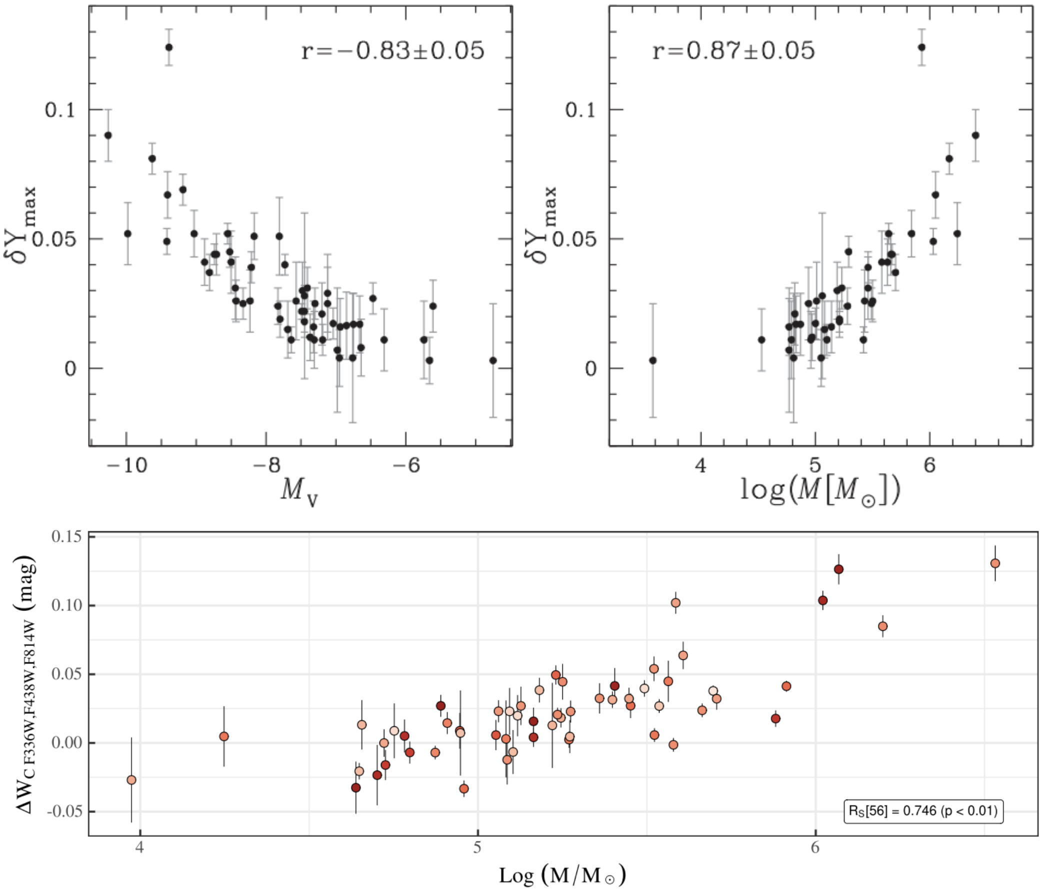

Figure 1.5: Upper panels: the plots show the maximum internal helium variation, as a function of the absolute magnitude (left) and the mass (right) of the host cluster (Milone et al., 2018a). Lower panel: normalized RGB width $\Delta W_{C F336W,\,F438W,\,F814W}$ plotted against the mass of the host cluster $log(M/M_{\odot})$ (Lagioia et al., 2019).

Helium Enhancement

After hydrogen, helium is the second most abundant element in stars. However, studying helium is challenging because, despite its abundance of around 25%, it is not always clearly visible in stellar spectra. Helium lines are detectable only in very hot stars, while they are difficult to identify in cooler stars. As the temperature decreases, the helium lines weaken and become undetectable. On the other hand, extremely hot stars experience internal mixing, which brings helium and other elements to the surface. Although this allows us to detect helium, the measured abundance is not representative of the star's original helium content due to the influence of convective motions. Therefore, only stars with temperatures in the range $8500\,K \leq T \leq 11300\,K$ are suitable for inferring the original helium abundance.

This issue is a significant challenge in modern astronomy because accurately measuring the initial element abundance of stars is crucial for testing the predictions of the Lambda Cold Dark Matter (ΛCDM) model. Alternative methods for measuring helium content exist (i.e., techniques like asteroseismology; see Verma et al. (2019)), but they are time-consuming due to the need for long exposures. Consequently, determining the helium content of stars remains a major challenge in modern astronomy.

Photometric diagrams, however, are sensitive to variations in helium among stars in GCs. Milone et al. (2012) proposed a new technique to infer the helium content of star clusters using these diagrams. This method involves comparing the diagrams with isochrones, generated with different helium content (see Figure 1.6), to derive the amount of helium of each different populations. An interesting aspect of this work (Milone et al., 2012) is that it was applied to NGC 6266, the same cluster analyzed in this thesis, to measure the helium content in its two extreme populations on the main sequence.

This technique has been applied to nearly all known GCs, revealing that the maximum helium variation is an intrinsic characteristic of each GCs, with values ranging from $0.01 \leq \Delta Y_{max} \leq 0.18$ (Zennaro et al., 2019; Milone et al., 2018a).

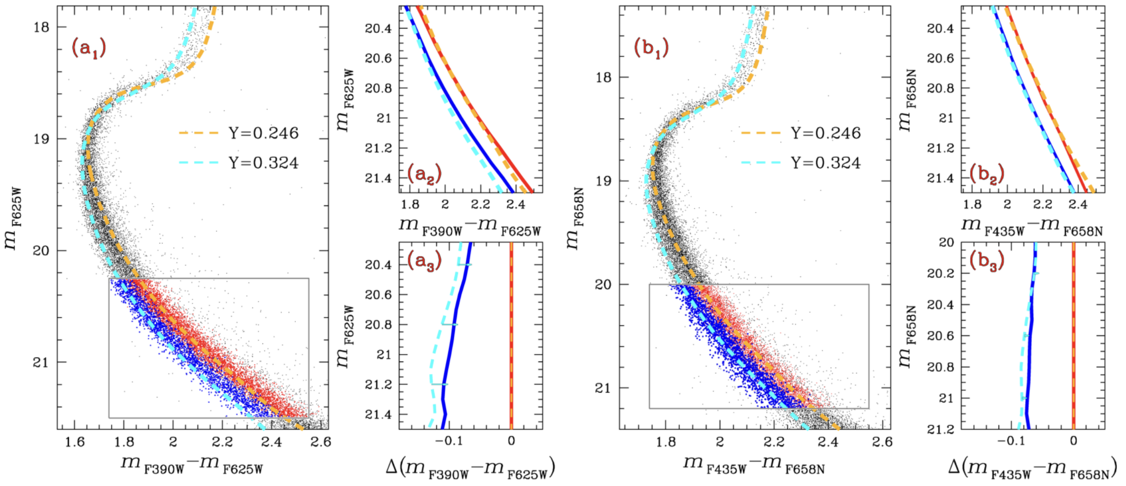

Figure 1.6: Optical CMDs of NGC 6266 from Milone et al. (2012). The orange and cyan lines represent the best fit isochrones inferred, with $Y = 0.246$ and 0.324, respectively.

Dependence on Globular Cluster orbit and Host Galaxy

According to some formation scenarios, GCs were initially more massive and comprised more stars than today. To explain their current masses, a significant fraction of stars from the outer part may have been lost through interaction with the Galaxy.

In this context, Zennaro et al. (2019) studied the content of 1P stars for a large sample of GCs. They found that clusters with larger perigalactic radii tend to host a greater fraction of 1P stars compared to those with smaller perigalactic radii, as shown in figure 1.7. This suggests that interactions with the Milky Way may influence the ratio between 1P and 2P.

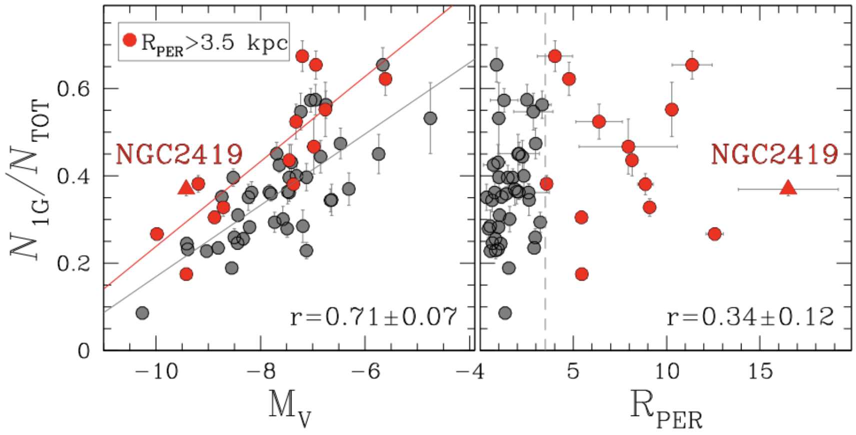

Figure 1.7: Fraction of 1P stars relative to the total number of analyzed stars as a function of absolute magnitude and perigalactic distance. The best-fit lines, shown in the left-hand panel, indicate that GCs with $R_{PER} > 3.5\,kpc$ have, on average, a larger fraction of 1P stars compared to the remaining GCs at a given luminosity (Zennaro et al., 2019).

No Dependence on Stellar Mass

Multiple stellar populations in GCs have been identified initially studying stars in the Red Giant Branch (RGB). Consequently, it became necessary to investigate the low-mass star region to determine whether the presence of these populations depends on the mass of the star. Using HST infrared observations, evidence for a split in the CMD sequence in the low mass star region was found (Milone et al., 2019).

Today, thanks to the James Webb Space Telescope (JWST), this region can be investigated with much greater precision than was possible with HST, allowing astronomers to reach the hydrogen-burning limit of the sequence.

Nevertheless, studying the lower main sequence of NGC 6752, Milone et al. (2019) found evidences of multiple populations among M-dwarfs, indicating that this phenomenon is independent from the stellar mass. Figure 1.8 shows this observations. The lower main sequence is well reproduced by isochrones generated with different CNO element abundances. Another study in the literature also addresses this topic; see Scalco et al. (2024).

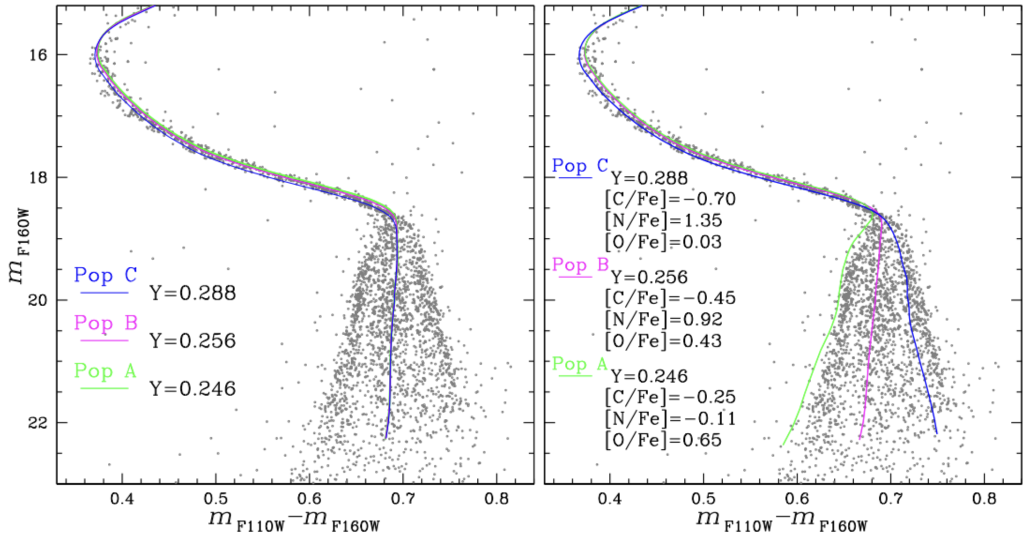

Figure 1.8: m_{F160W} vs $m_{F110W} - m_{F160W}$ CMDs of NGC 6752. The colored lines represent isochrones with varying helium content alone (left) and isochrones with different helium content plus various CNO products (right). From Milone et al. (2019).

More Centrally Concentrated second population Stars

According to many scenarios for the formation of GCs, 2P stars should originate in the central region of the cluster. Therefore, we expect to observe a non-uniform distribution of 2P stars as a function of the radial distance from the cluster center.
The best instrument for studying this issue is the Gaia satellite, which can investigate clusters reaching their outer regions, overcoming the limited Field of View (FoV) of HST. However, these observations depends on the dynamical age of the cluster: dynamically young clusters preserve more information on their initial conditions, while dynamical old clusters can be completely mixed already, erasing this information. As shown in figure 1.9, some GCs, such as 47 Tucanae and NGC 3201, exhibit an higher concentration of 2P stars in the innermost regions of the cluster, while others, such as NGC 6752 and NGC 6121 show a uniform distribution of 2P stars Mehta et al. (2024).

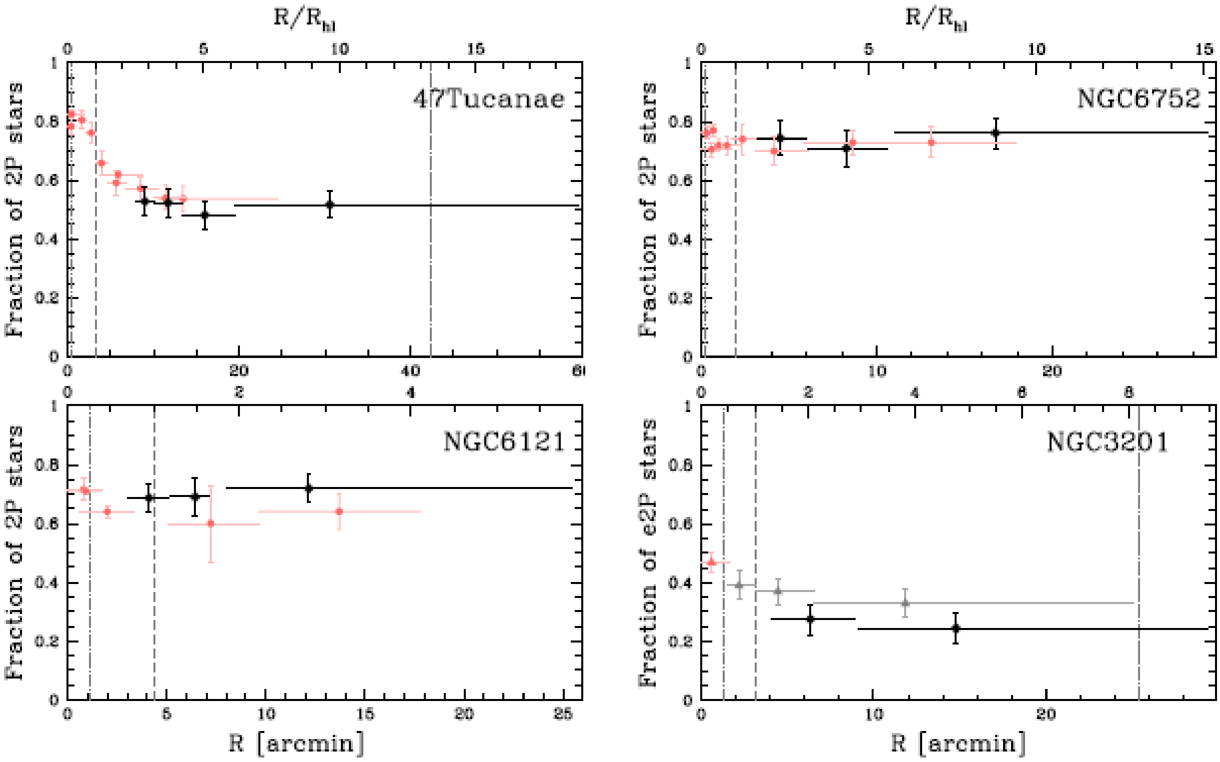

Figure 1.9: Radial distribution of 2P stars based on Gaia data analysis by (Mehta et al., 2024). The GCs NGC 6752 and NGC 6121 show a uniform distribution of 2P stars, while 47 Tucanae and NGC 3201 exhibit a more centrally concentrated fraction of 2P stars.

Supernovae contribution and Hot-Hydrogen burning cycle

Apart from type II GCs, no significant iron variations have been detected between 1P and 2P in GCs (Marino et al., 2019). This suggests that supernova Ia events did not play a crucial role in the synthesis of 2P stars. This is likely because GCs do not have sufficient gravitational power to retain the material ejected into the intra-cluster medium by the violent explosions of supernovae.
The only chemical differences observed so far among type I GCs are related to the content of light elements. Specifically, the 2P of stars show enhanced levels of elements like He, N, Na, and Al, while being depleted in C, O, and Mg (Marino et al., 2019). These anticorrelations suggest that processes such as the CNO cycle and proton-capture reactions may be responsible for the "*anomalous*" chemical composition observed in 2P stars.

Chapter 2

Formation Scenarios of Globular Clusters and Kinematic Implications

In this chapter, I will discuss about the formation scenarios of GCs, which are broadly divided into multi-generation and single-generation scenarios. First, I will discuss multi-generation scenarios, focusing particularly on the Asymptotic Giant Branch model. Next, I will explore single-generation scenarios, which propose that all stars in a GC form in a single burst of star formation. Then, I will also discuss about formation scenarios of anomalous GCs. Finally, I will examine the implications of these models on the kinematics of stars within GCs.

2.1 Multiple Generation Scenarios

Multi-generation scenarios propose that GCs form through multiple episodes of star formation. In this model, an initial generation of stars forms, and their evolution creates the conditions for subsequent generations to form from enriched material. One of the most well-studied multi-generation scenarios is the Asymptotic Giant Branch (AGB) model proposed by Ventura et al. (2001). This scenario investigates the hypothesis of a self-pollution mechanism in GCs, driven by intermediate-mass stars during their AGB phase. These stars eject processed materials into the intra-cluster medium through strong stellar winds. They are considered key polluters because their dominant nucleosynthesis process, the CNO cycle, enriches the stars with helium and nitrogen while depleting carbon and oxygen, matching the chemical patterns observed in second-generation stars.
Once ejected into the intra-cluster medium, this material mixes with the pristine material that survived from the formation of the first generation of stars. It then cools down and collapses towards the inner part of the cluster, leading to the formation of second-generation stars.

Another well-known multi-generation model is the Fast Rotating Massive Star (FRMS) model, initially proposed by Decressin et al. (2007) and later refined by Krause et al. (2013). According to this scenario, the enrichment of 2P stars in GCs originates from material ejected into the intra-cluster medium by fast-rotating massive stars ($20 - 120\,M_\odot$) during their main sequence or early post-main sequence phases. Due to their rapid rotation, these stars experience strong internal mixing, leading to the ejection of chemically processed material through stellar winds or equatorial decretion disks. This processed material exhibits the chemical patterns characteristic of present-day GCs, such as the Na-O, N-C, and Al-Mg anticorrelations. The ejected material subsequently cools and mixes with the pristine gas remaining in the cluster, ultimately forming 2P stars.

If these scenarios proves correct, they would have significant cosmological implications for the assembly of the Milky Way. Multi-generation scenarios, unlike single-generation scenarios, do not directly address the **mass budget problem**: the observed discrepancy between the number of first-generation stars observed, and the one we expect to account for the number of second-generation stars.

2.1.1 Mass-budget problem

By studying the distribution of stars in GCs, astronomers have observed that 2P stars represent the dominant component. This is a crucial observation for understanding the origin of GCs, as multi-generation scenarios suggest that only a small fraction—around 5%—of the initial first-generation mass (Renzini, 2013) has the necessary conditions to form second-generation stars.
In particular, Renzini (2013) estimated that the original mass of a primordial GCs can be calculated as:

$$M_{\mathbf{progenitor}} \approx M_{\mathrm{SG(today)}} \times 20 \times \epsilon$$

where $M_{\mathrm{SG(today)}}$ is the mass of the second-generation stars as measured today, the factor of 20 accounts for the fact that only 5% of 1P stars have the right characteristics to pollute the material from which second-generation stars were born, and ϵ represents the star formation efficiency.
It is important to note that, by multiplying this mass by 200—which is approximately the number of GCs in the Milky Way—we obtain a total mass of around $4 \times 10^9\,M_\odot$. This suggests that a significant amount of mass has been lost into the Galactic halo over time to account for the masses of GCs we observe today.
This issue is referred to as the **Mass-budget problem**, and a possible solution proposes that GCs were much more massive in their early stages than they are today. Over time, through interactions with the host galaxy, they lost the majority of their first-generation stars, contributing significantly to the stellar population of the Galactic halo.

2.2 Single Generation Scenarios

Single-generation scenarios propose that all stars within a GCs form in a single, rapid burst of star formation. According to this model, the observed chemical inhomogeneities among multiple populations are not the result of successive star formation events but rather the consequence of exotic physical processes that happened during the formation of the cluster.
One example, as described by Gieles et al. (2018), identifies the polluter as a Super Massive Star (SMS) that, through its strong stellar winds, releases processed materials rich in helium, nitrogen, and sodium into the cluster.
The model predicts the formation of a SMS with a mass on the order of $10^3\,M_\odot$ in the central region of the cluster, resulting from stellar collisions in the dense environment. Young clusters have sufficient gravitational power to retain the material ejected by these SMSs which are then acquired by cluster's member stars through accretion processes. This model aligns with observations of chemical inhomogeneities between the first and second generations of stars, presenting a valid alternative to multi-generation scenarios. Figure 2.1 shows a schematic representation of this scenario.

An important consequence of this model is that the SMS, due to its enormous size and brief life, could lead to the formation of an intermediate-mass black hole in the cluster center. The existence of such black holes is currently a debated topic in astronomy and astrophysics (Noyola et al., 2008; Van der Marel and Anderson, 2010).

Moreover, another well-known single-generation scenario is the Early Disc Accretion in Massive Interacting Binaries (MIB) model, proposed by Bastian et al. (2013). According to this model, the polluters are massive binary systems that, due to their mutual interactions such as mass transfer, mergers, or stellar winds, eject chemically processed material into the cluster. This material is then accreted by the formation disks of pre-MS stars, which are formed within the same generation, thus making this a single-generation model. These pre-MS stars, having very low mass, have not yet reached the main sequence, and the accreted material alters their chemical composition.

Although these scenarios address several issues present in the multi-generation models, such as the mass-budget problem, they also have some significant shortcomings, such as the prediction that, since the accretion rate depends on stellar mass, chemical anomalies should be observed between high- and low-mass stars. However, such anomalies are not observed (Milone et al., 2018a; Ziliotto et al., 2023).

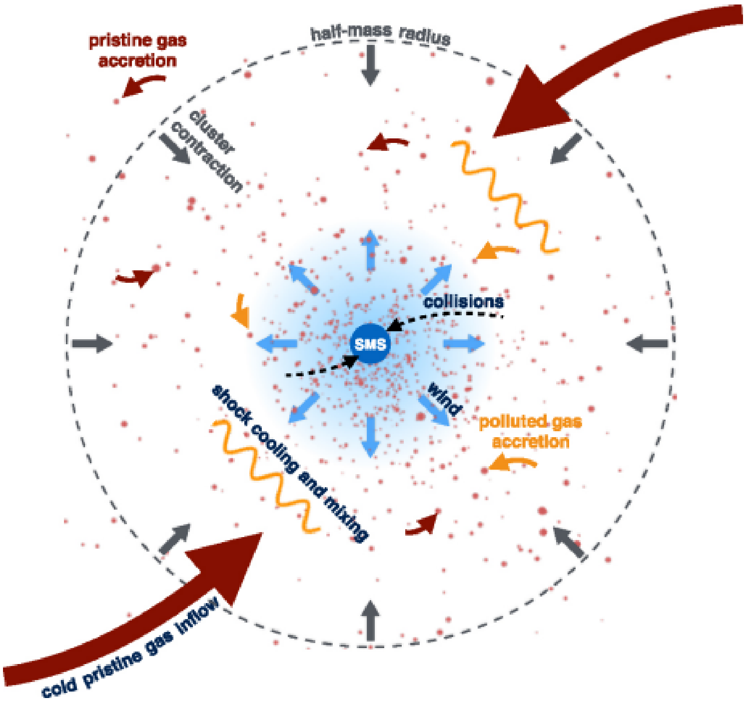

Figure 2.1: A model for SMSs is shown in Gieles et al. (2018). In this illustration, the SMS is located at the center. Blue arrows represent the stellar winds emanating from the star, while red arrows indicate the infalling gas that enables the star to gain mass.

2.3 Anomalous Globular Clusters

The final formation scenario of GCs I will review concerns Anomalous Globular Cluster (AGC), defined in section 1 as the class of GCs that present an additional sequence of stars in their chromosome map. Bekki and Tsujimoto (2016) discuss the origin of AGCs, suggesting that these clusters originated within dwarf galaxies that were later accreted by the Milky Way. Once captured by the Milky Way, these dwarf galaxies were disrupted by the strong tidal forces generated by the host galaxy, leaving behind the GCs as remnants.

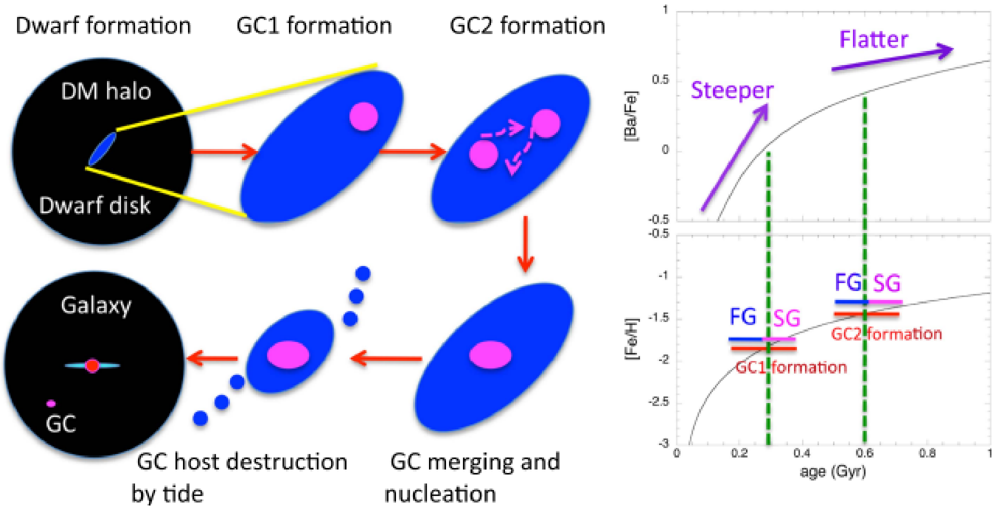

Figure 2.2: The illustration from Bekki and Tsujimoto (2016) shows the process of GCs merging. GC1 and GC2 form within a dwarf galaxy embedded in a massive dark matter halo at different epochs. The two clusters then evolve and interact, merging into a single object in the nuclear region of the galaxy. Later, the dwarf galaxy interacts with the host galaxy, is disrupted, and what remains from the disruption becomes the AGC we observe today in the Galactic halo.

This model can be seen as an extension of the multi-generation scenarios because it predicts that GCs acquire their metallicity spread through distinct episodes of star formation that occurred in the progenitor dwarf galaxy. The intra-Galactic material is enriched by stellar feedback processes such as supernova explosions and stellar winds. Unlike the scenario proposed by Ventura et al. (2001), where stellar winds are the primary polluters, this model allows supernovae to act as polluters, as the strong gravitational field of the galaxy and its dark matter halo can retain the material ejected by the supernovae.

According to their model, if the original dwarf galaxy is massive enough, it can lead to the formation of GCs with multiple populations. If the timescale for GCs merging within the GC-host dwarf galaxy (t_{merge}) is shorter than the destruction timescale of the GC-host dwarf t_{dest} due to the Galactic tidal field during the accretion process, then various GCs within the dwarf galaxy can interact and merge to form an AGC. On the other hand, if t_{merge} is longer than t_{dest}, GCs are stripped out from their host dwarf galaxy before they can merge and become an AGC. Simulations indicate that the more massive a GCs is and the shorter its dynamical timescale, the higher its probability of becoming anomalous.

2.4 Kinematics and Clusters Origin

The different formation scenarios for GCs have significant implications for the kinematics of the stars within these clusters. In multi-generation scenarios, the second generations of stars form from gas that may have dissipated energy and settled into a more centrally concentrated configuration. As a result, these stars might exhibit different kinematic properties compared to the first-generation stars, such as lower velocity dispersion and a more centrally concentrated spatial distribution (Vesperini et al., 2013, 2014, 2021). This variation occurs because each distinct episode of star formation happens under slightly different dynamic conditions. For instance, in the AGB scenario, the material that forms the second generation of stars collapses towards the central region, acquiring more homogeneous rotational properties compared to the first generation of stars, which simply reflect the dynamical characteristics of the primordial cloud.

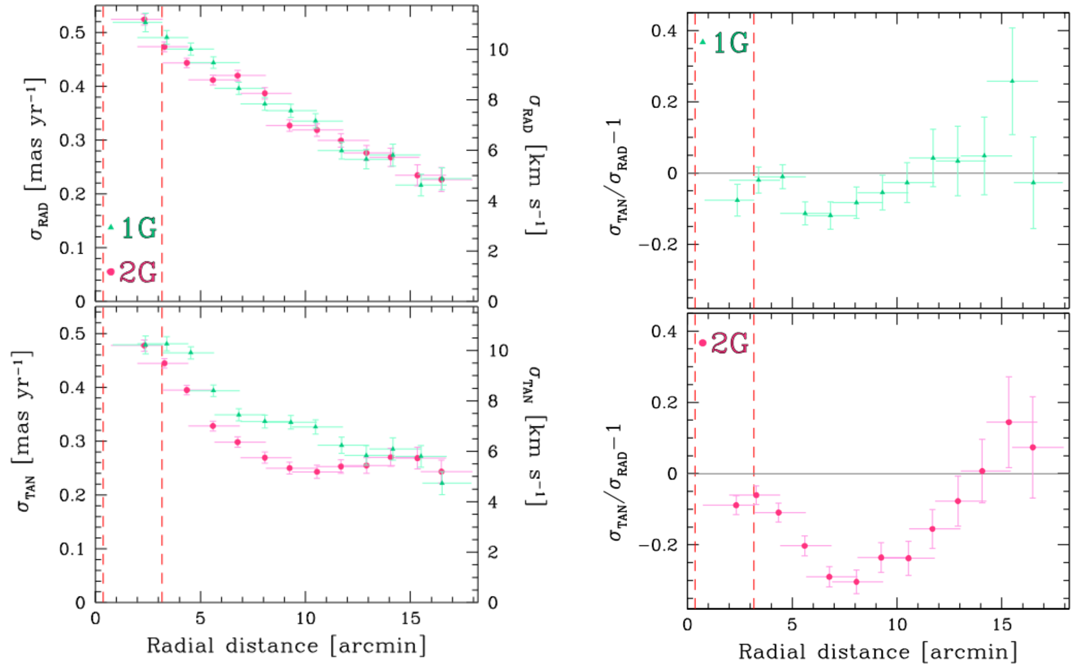

Figure 2.3: Left panel: radial and tangential velocity dispersion profile, as a function of the distance from the Galactic center, for the Galactic GCs 47 Tucanae. Right panel: tangential to radial isotropy for 1G (top) and 2G stars (bottom) as a function of the distance from the cluster's center (Milone et al., 2018b).

This kinematic pattern is similar to what we expect for AGCs. As discussed in the previous section, the model proposed by Bekki and Tsujimoto (2016) is essentially a multi-generation scenario. The

key difference is that, in the case of AGCs, the merging processes in the nucleus of the dwarf galaxy and later with the host galaxy may cancel out the primordial kinematic signatures, at least in the inner part of the cluster.
In single-generation scenarios, all stars form simultaneously from the same primordial cloud, leading to more uniform kinematic properties across the cluster. However, early dynamical evolution and relaxation processes can still introduce some kinematic signatures, though this would be less pronounced than in multi-generation scenarios.

By studying the kinematics of stars in GCs, we can gain insights into their formation histories. Understanding these kinematic signatures is crucial for unraveling the complex formation histories of GCs and determining the role they played in the evolution of the galaxy.
Pioneering studies based on a few GCs have investigated this topic (Milone et al., 2018b; Cordoni et al., 2020, 2024), showing that it is possible to detect kinematic differences between the two populations. For example, Milone et al. (2018b) demonstrated that the two stellar populations in 47 Tucanae exhibit different dispersion velocity profiles concerning the tangential velocity component. The results of their study are compatible with the possibility that the two populations formed in distinct episodes of star formation. Cordoni et al. (2020, 2024) extended this study to several GCs, finding similar results.

2.5 Outline and purpose of the thesis

The purpose of this thesis is to extend the current sample (Milone et al., 2018b; Cordoni et al., 2020, 2024) of analyzed GCs, by studying the internal kinematics of the Galactic GC NGC 6266. For the first time, I will examine the kinematics of its multiple populations, aiming to shed light on the mystery behind GCs formation. Unlike other studies in the literature, I used HST data instead of Gaia data. While this choice has the disadvantage of covering a smaller FoV, it offers the significant advantage of higher resolution, which greatly improves the number of observed stars, the quality of the ChM, and the accuracy of the proper motions.

In chapter 3, I will describe the dataset and the data reduction procedure that I followed to derive the photometric and astrometric catalogues for NGC 6266. In chapter 4, I will present the data analysis, including the separation of the two populations using the chromosome map and the kinematic analysis of the stars in each population. Finally, in chapter 5, I will present the results of my analysis and discuss their implications in the context of GCs formation scenarios.

Chapter 3

Dataset and Data Reduction

In this chapter, the methods used for data reduction will be presented. In the first part, I will introduce the dataset, briefly describing the instrumentation used to collect the data. In the second part, I will discuss the creation of the photometric and astrometric catalogues, both obtained applying the effective point-spread function technique by J. Anderson and collaborators.

3.1 Instrumentation

All the data analyzed in this thesis come from images collected using the HST. This powerful telescope has been orbiting Earth since 1990, and with its 2.4 m mirror, it has revolutionized astronomy[1]. Being outside Earth's atmosphere, HST has the significant advantage of being immune to atmospheric distortion, allowing it to produce diffraction-limited images. For this reason, it is an ideal instrument for capturing precise images of crowded stellar regions, such as GCs. Furthermore, its ability to observe in the near-ultraviolet region was crucial in the discovery of the multiple populations phenomena. In this part of the spectrum, we can distinguish stars with a different chemical composition, particularly regarding light elements.

HST is equipped with five main instruments that allow for study of the Universe across a wide range of wavelengths, from near-ultraviolet to near-infrared. The instruments used in this work are:

- Wide Field Camera 3 (WFC3), using the **UVIS** channel, which observes wavelengths between 2000Å and 10000 Å;
- Advanced Camera for Surveys (ACS), using the **WFC** channel, which observes wavelengths between 3500 Å and 11000 Å.

3.2 Dataset

In this thesis, I worked with the astro-photometric catalogue of NGC 6266, obtained by analyzing images from the Hubble archive[2]. The available images are listed in the following table:

Date	N × Exptime	Instrument	Filter	Program	Pi
01/08/2004	$200s + 2 \times 340s$	ACS/WFC	F435W	10120	S. Anderson
01/08/2004	$30s + 120s + 3 \times 340s$	ACS/WFC	F625W	10120	S. Anderson
01/08/2004	$340s + 3 \times 350s + 3 \times 365s + 3 \times 375s$	ACS/WFC	F658N	10120	S. Anderson
18/06/2010	$4 \times 35s + 5 \times 393s + 5 \times 421s$	WFC3/UVIS	F390W	11609	J. Chaname

Table 3.1: Information about the archive images of NGC 6266.

---

[1] https://science.nasa.gov/mission/hubble/overview/hubbles-30th-anniversary/

[2] https://archive.stsci.edu/

These datasets investigate a region of $2.6\,arcmin^2$ around the astronomical coordinates (RA, Dec) = $(17:01:12.000, -30:06:29.50)$, as shown in figure 3.1. This is an ideal region for the purpose of this thesis, as it allows us to study the kinematic behavior of stars in multiple populations near the half-light radius, which is $r_{hl} = 0.92\,arcmin$ (Baumgardt and Hilker, 2018) from the cluster center, where simulations predict observable kinematic differences between the two populations.
After downloading all the images from the MAST archive[3], I performed the data reduction process, following the procedure developed by Anderson et al. (2008). This method is based on Point Spread Function (PSF) photometry, which I will explain in the following sections. All the steps described in the rest of the chapter have been applied individually to all the filters reported in table 3.1.

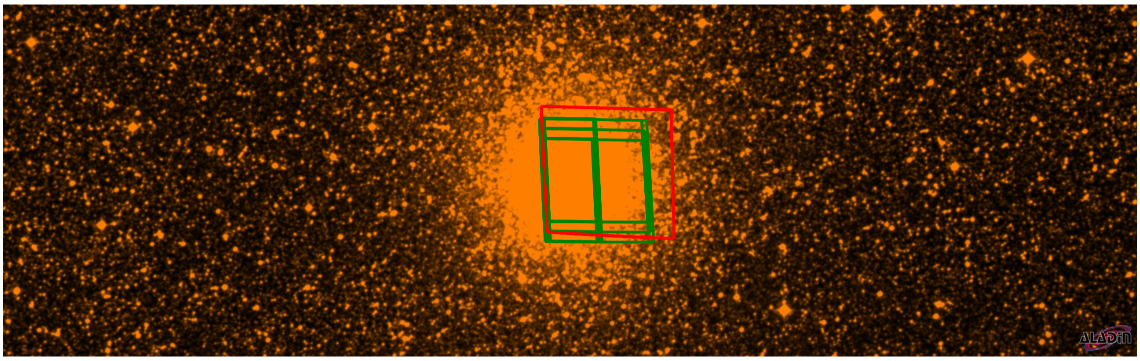

Figure 3.1: Footprints of the HST images for the filters in table 3.1, which I reduced in this work. Footprints were obtained from (Bonnarel et al., 2000).

Both the WFC3/UVIS and ACS/WFC cameras are equipped with two Charge-Coupled Device (CCD) placed side by side (each with 2048×4096 pixels^2). The images of the two CCDs are merged and saved in single `fits` file using the `FORTRAN`[4] code `img2wjc`, which creates a single image with dimensions 4096×4096 pixels^2.

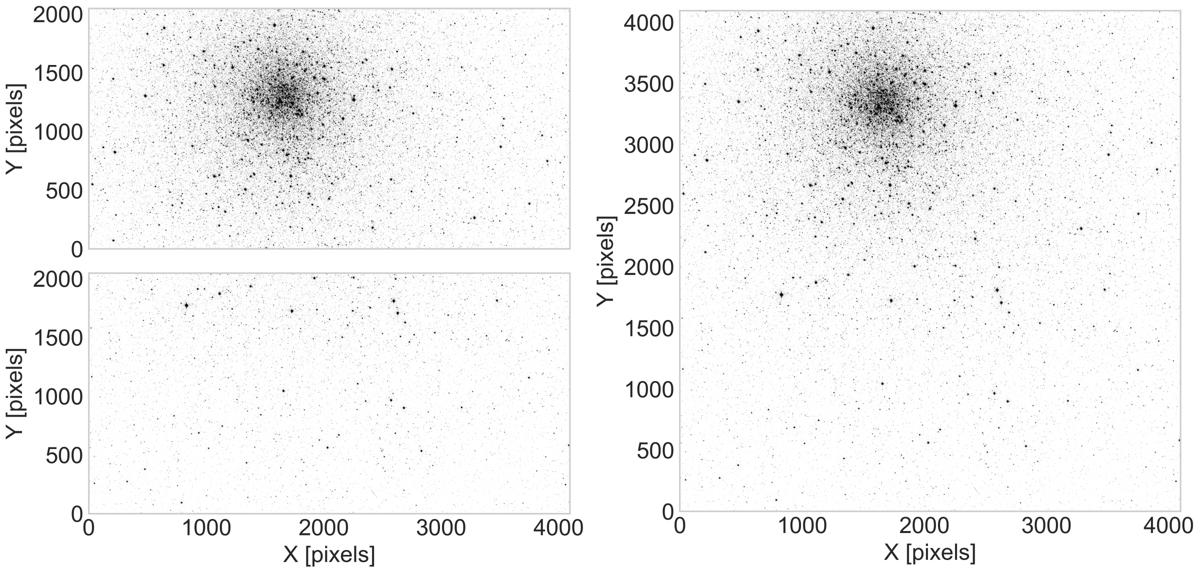

Figure 3.2: The two figures on the left represent the two images of the GC NGC 6266 collected by the two different CCDs of the HST camera. On the right, we can see how the final image appears after being processed by the `img2wjc` code.

---

[3] https://mast.stsci.edu/search/ui/#/hst/results?resolve=true&target=NGC%206266&data_type=image&observations=S&active_instruments=acs,wfc3&legacy_instruments=&radius=3&radius_units=arcminutes&useStore=false&search_key=3404c2282c614

[4] https://fortran-lang.org/

3.3 Point Spread Function

When the light coming from a star is collected by the CCD, it appears as a point-like source. To accurately estimate the stars magnitude and position on the CCD, which is fundamental for deriving proper motions, we use a PSF model. A PSF model is defined as the response of a focused optical imaging system to a point-like source.
This function is the result of the convolution of two functions: $\psi_E = \psi_1 \otimes \Pi_{\mathrm{CCD}}$. The first function ($\psi_1$) is the instrumental PSF (iPSF), which provides the flux for a point source as a function of the offset from its center. The second function, Π_{CCD}, is the **pixel response function**, representing the sensitivity of the detector at each point of the pixel. Unfortunately, these functions are not directly observable. To address this, Anderson and King (2000); Anderson et al. (2008) proposed a new approach based on the concept of the effective PSF (ePSF).
The ePSF is a continuous function that depends on the offset from the center of the PSF, and its value at any point gives the fraction of light from a point source that would fall within a pixel centered at that point. One of the major challenges with this technique is that the choice of the PSF model used to fit the stellar profile significantly affect the result. Even a slight inaccuracy in the model can induce systematic errors in the measurements.

To resolve this issue, Anderson and King (2000); Anderson et al. (2008) developed a method that constructs the PSF directly from the target image using a numerical approach. The first step involves using a library PSF model, based on the characteristics of the CCD and the specific filter being analyzed (this procedure is repeated for each filter individually). This initial model serves as the starting point for the PSF in our image. The `FORTRAN` routine `img2psf` then applies this model to isolated, non-saturated stars in the image. The residuals from the fit are used to refine the PSF, generating an updated version. This iterative process continues, with each new PSF being applied to the data, until the residuals between input and output become negligible. In this way, the method directly constructs an accurate PSF model from the data.
This `FORTRAN` routine takes seven parameters:

```
img2psf HMIN FMIN PMAX QMAX NSIDEs PSFFILE IMG.fits
```

- **HMIN** defines the minimum distance (in pixels) between two stars to consider them for the PSF computation. In my analysis, I used a value of 13 to ensure that only isolated objects were considered;

- **FMIN** defines the minimum number of counts required to consider a pixel as part of a star rather than background noise. To exclude faint objects from the PSF calculation, I set this value to 5000;

- **PMAX** defines the maximum number of counts per pixel to exclude saturated stars. This is based on the saturation limit of the CCD pixels, which for HST is equal to 54000 *counts*;

- **QMAX** is a quality flag value that indicates the goodness of the fit. It is used to distinguish stars from other objects like galaxies or cosmic rays. I set this to 0.3 in my analysis;

- **NSIDEs** defines the number of regions into which the image is divided, with a separate PSF computed for each. I set this to 3;

- **PSFFILE** specifies the PSF model to be used as a preliminary guess at each iteration;

- **IMG.fits** specifies the image on which the PSF is computed.

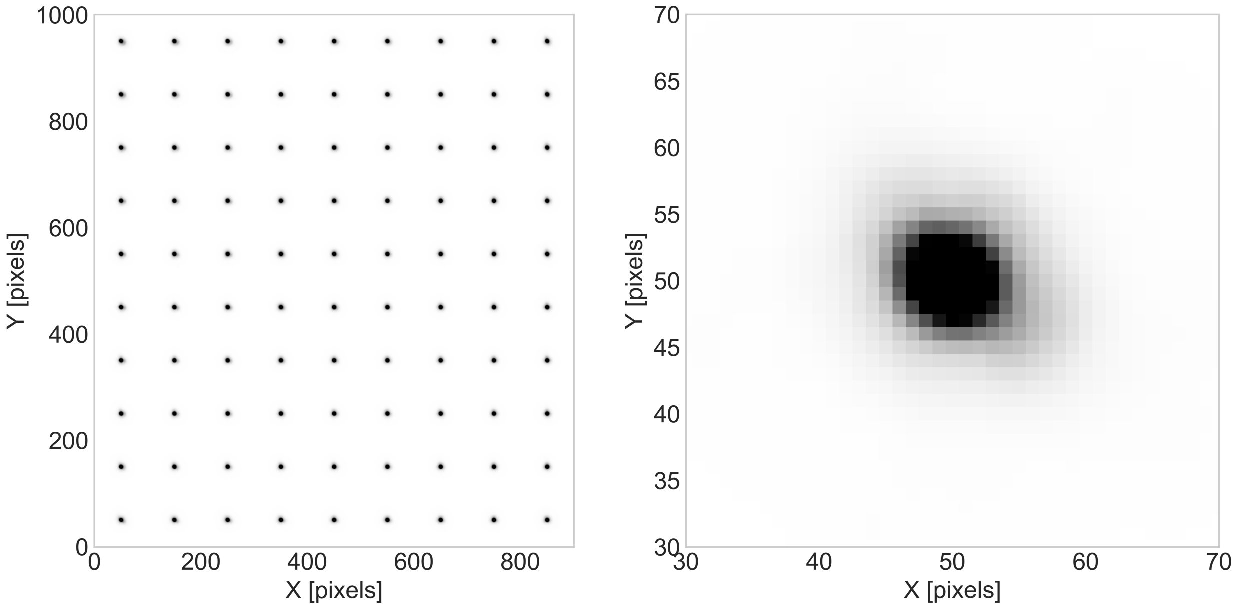

Figure 3.3: This figure shows the PSF model obtained from `img2psf`. Left: PSF model obtained for one exposure in the HST filer F390W. Right: a zoom-in on a single PSF model.

The output file of this procedure is shown in figure 3.3. It is saved as `_PSF.fits` and represents the PSF model built for the processed image. As seen in the output, the program doesn't produce a single PSF but rather a grid (9×10) of PSFs. This is because the PSF may vary slightly depending on the position within the detector due to sensitivity variations. Using a grid of PSF significantly improves the accuracy of the measurements.

The next step of the analysis involves using another `FORTRAN` routine, `img2xym`, to measure fluxes and positions of each star using the derived PSF. The input parameters of this code are:

```
img2xym HMIN FMIN PMAX PSFFILE IMG.fits
```

The meaning of the parameters is the same as before, but now we are interested in measuring the positions and fluxes for all objects in the image, so the parameters of the code need to be adjusted. Specifically:

- **HMIN** is set to 5;
- **FMIN** is set around 50 to include faint objects;
- **PMAX** is set to a very high value (9999999) to include saturated stars.

At the end of this procedure, an `ascii` file is generated, containing the position, magnitude, and Qfit for all detected sources. The Qfit parameter indicates how well the position and magnitude were measured. Since the program cannot distinguish between real stars and false signals, Qfit is used to filter out false detections. This is possible because Qfit exhibit a strong correlation with magnitude, as seen in figure 3.4.
In the Qfit vs magnitude plot, well-measured stars occupy the orange and red regions, while blue objects represent non-stellar detections and poorly measured stars. In the plot I highlight with red all saturated stars, because due to the saturation of the pixel their photometry is poor. The following ptocedure was used to identify the *stellar region*:

1. I selected objects with magnitudes between -13.5 and -6, as outside this range, the Qfit-magnitude relationship becomes less reliable;
2. For magnitudes in this range, I divided the interval into sub-samples, calculated the mean and dispersion (σ) for each, and plotted the mean with 3σ added to define the orange region. This last process was repeated with a smaller region around the centroid to better define the trend.

Finally, I generated a new output file for each image and filter, containing the position, magnitude, and Qfit values for the selected stars.

So far, I described the procedure used to obtain accurate position and magnitude measurements from raw images. I derived the best PSF model for each image. Although I did not distinguish between the two instruments (WFC3/UVIS and ACS/WFC) during the explanation, it's important to note that there are different versions of the codes used, optimized for each of the specific instrument.

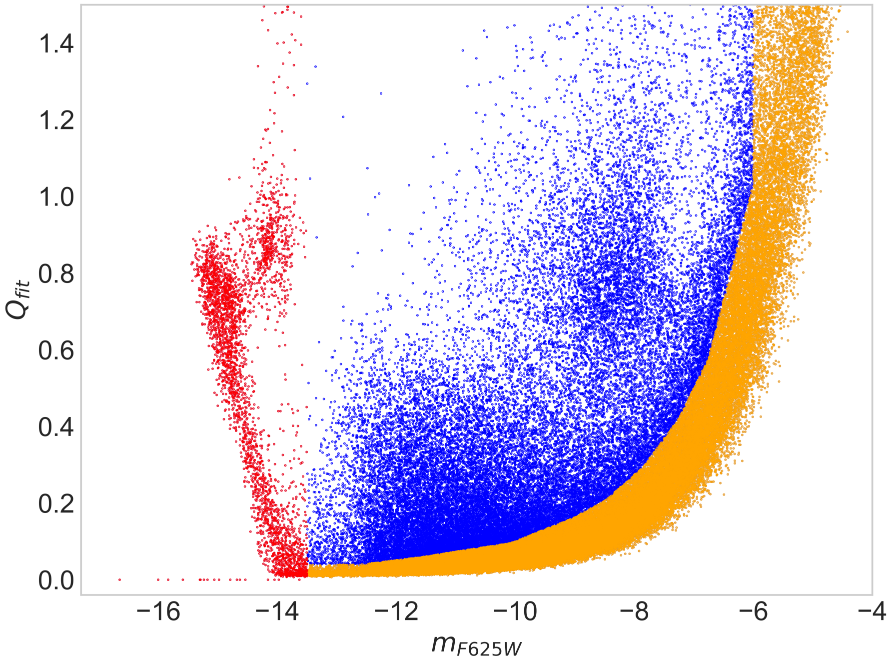

Figure 3.4: Procedure to distinguish candidate stars from poorly measured objects: every point in the Qfit vs. m_{F625W} diagram represents an object measured by the code. Orange dots correspond to stars, while red dots indicate saturated stars, whose photometry is suboptimal, as shown by the increase in the Qfit value. Blue dots represent poorly measured detections. This example refers to an image taken with the F625W filter.

3.4 Photometric Catalogue

Now that we have derived the positions and magnitudes of each star across different filters, we can build a **photometric catalogue**, which combines this information into a single dataset. The process of creating such a catalogue is complex due to the different times, orientations, and sometimes even areas of the cluster covered by each image. Thus, the first step is aligning all images to a common reference frame.

To do this, we use the `FORTRAN` routine `xym2mat`, which aligns all images to a selected reference frame, or `master frame`. This master frame serves as the reference for all the subsequent transformations and it is selected as the image with the biggest exposure time among the available ones. I begin by creating a file, `IN.xym2mat`, which list the images and their relevant parameters in the following format:

```
0000 "image.xym" c0 f0 "m-99,-11"
```

here, the first value represents a sequential number (starting from 0000 for the master image), the second value specifies the image filename, the third identifies the camera used, the fourth refers to the filter, and the last value defines the magnitude range of the stars used for the alignments. We need to specify to the code the camera and the filter used because the code applies the proper distortion corrections to all images.

The transformation of coordinates between images is determined using bright stars common to all frames. This method is known as **Cross Identification** and relies on constructing **triangles** of stars in the master frame and identify the corresponding triangles in other images. The transformation between the two coordinate system is calculated using least-square fitting of the following equations:

$$\begin{cases} x_1 = \alpha + \gamma \cdot x_2 + \epsilon \cdot y_2 \\ y_1 = \beta + \delta \cdot x_2 + \xi \cdot y_2 \end{cases}$$

where (x_1, y_1) are the coordinates in the master frame, (x_2, y_2) are the corresponding coordinates in the other image, and α, β, γ, δ, ϵ, ξ are the transformation coefficients.

After the first iteration, which uses bright stars (even saturated ones) to establish the initial transformation, I perform a second iteration excluding saturated stars for a more precise fit. This is done by modifying the magnitude range in the `IN.xym2mat` file.

The output includes a series of `MAT.XXX` files, where each of them contains positions, residuals[5] and magnitudes for stars in the corresponding image. To verify the accuracy of the transformation, I examined the residuals as shown in figure 3.5. The residuals should follow a nearly circular distribution centered at zero. The average dispersion of these residuals, calculated as the $68^{\text{th}}-$percentile, is compared with pre-determined values from the `FORTRAN` code, and used as an input for the second iteration. The code also generate the `TRANS.xym2mat` file, which contains the transformation coefficients just determined; in this way the second iteration starts from an initial guess and tries to improve their values.

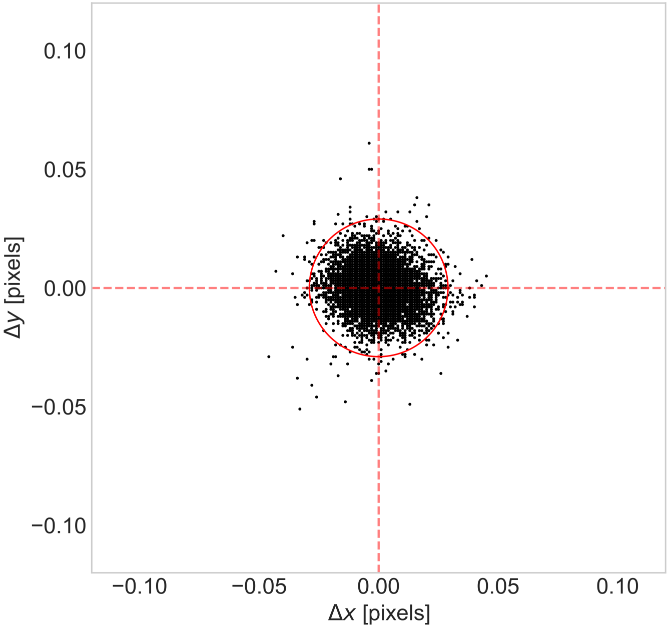

Figure 3.5: Quality check to verify the accuracy of the transformation obtained using the `xym2mat` code. The dots in the figure represent the residuals of the transformation. If the points are clustered symmetrically around zero, it indicates that the code has successfully determined the correct transformation coefficients. In the case of a failed computation, the points will be randomly distributed in the plot.

The next step is creating individual catalogues for each filter, using the routine `xym2bar`. This program averages the positions and magnitudes of each star across all images for a given filter, weighting the averages based on the exposure time of each image. The input file `IN.xym2bar` is similar to `IN.xym2mat`, except that the line for the master frame is omitted. I also provide the code a parameter, that specifies the minimum number of images in which a star must appear to be included in the catalogue. For my analysis, I set this parameter to 1, as some filters had a limited image data.

The average in magnitudes must account for different exposure time, so I adjust the magnitude range in the input file according to:

- For short exposures, saturated stars are included since they are less affected by saturation compared to long exposures;

---

[5] Defined as the difference between the position of the star in the master frame and the position of the star in the analyzed image.

- For long exposures, stars with magnitudes between −13.5 and −4.5 are used, removing both saturated and faint stars. The latter are better measured by other methods.

The output is a catalogue for each filter, containing star positions, magnitudes, the number of images in which the star was identified, and the number of images in which its magnitude was measured.

Once I have individual catalogues for each filter, the next step is to match them so that each row corresponds to the same star across all filters. This is done with the `xym1mat` routine, which functions similarly to `xym2mat`. I select a reference filter (F625W in this case) and use cross-identification to recognize stars across the different filters. As before, the routine first aligns bright stars, calculates a first guess for the transformation, and then refines it using all stars.
At this stage, the positions are still in the reference frame of the F625W filter. To convert them to an absolute reference frame aligned with Right Ascension (RA) and Declination (DEC), I matched my catalogue with data from the Gaia mission, which provides highly accurate positions in the RA-DEC coordinate system (GaiaCollaboration, 2018). After obtaining the Gaia catalogue for NGC 6266 by downloading the data from the Gaia project website[6], I matched it to the F625W frame using the transformation procedure described earlier. For this, the Gaia catalogue was projected onto the plane tangent to the cluster center. This projection was performed using a `SuperMongo`[7] script provided by my research group, the GALFOR[8] team. Once the F625W filter was aligned with the Gaia frame, it became the new master frame, and the other filters were subsequently matched to it.

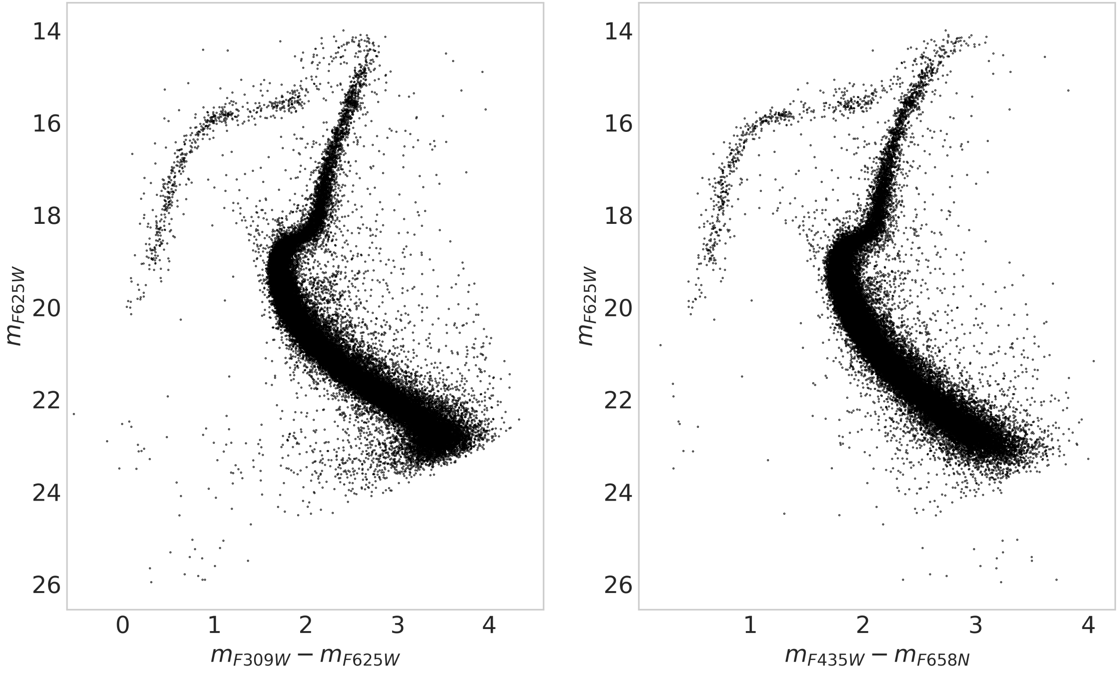

Figure 3.6: Preliminary CMDs created after matching the catalogues. The left CMD is generated using the $m_{F390W} - m_{F625W}$ color, while the right one uses the $m_{F435W} - m_{658N}$ color. In both cases, the colors are plotted against the m_{F625W} filter. These plots still need to be corrected for field star contamination and differential reddening.

The final result is a matched photometric catalogue for each filter, which serves as the basis for constructing a preliminary Color-Magnitude Diagram (CMD), as shown in Figure 3.6. The magnitudes obtained at this stage are **instrumental magnitudes**, meaning they have not yet been converted to the **Vega** system (Johnson, 1955), which is commonly used for comparison with other works. Instrumental magnitude is defined as

$$m_{\text{instrumental}} = -2.5 \log_{10} (\text{counts}) \tag{3.1}$$

---

[6] https://www.cosmos.esa.int/web/gaia/dr3

[7] https://www.astro.princeton.edu/~rhl/sm/

[8] https://progetti.dfa.unipd.it/GALFOR/

where “*counts*” represents the total number of electrons collected in the area of the CCD modeled by the PSF as corresponding to the star’s flux.

To convert these instrumental magnitudes to the Vega system, I applied the zero-point magnitudes calculated according to Milone (2015), as listed in Table 3.2.

	F390W	F435W	F625W	F658N
Zero Point	31.567	32.0688	31.9740	28.7413

Table 3.2: Zero-point magnitudes for GC NGC 6266 photometry, from Milone (2015).

3.5 Astrometric Catalogue

The goal of this thesis is to study the internal kinematics of the Galactic GC NGC 6266, specifically by measuring the proper motions of its stars. In the previous sections, I explained how to accurately derive the positions and magnitudes of stars in various photometric filters, and how these were aligned into a common reference frame for comparison.
While the photometric catalogue was produced by myself, the astrometric catalogue was provided by the GALFOR group. Nevertheless, I will briefly explain how it was obtained and outline the main steps of the analysis.

To measure proper motions, it is crucial to have images taken at different epochs, as proper motion is determined by comparing the positions of stars over time. As noted in table 3.1, there is a six-year gap between the acquisition of images in the F435W, F625W, and F658N filters and those in the F390W filter. This time span is sufficient to determine the stars proper motions.
However, the method used in the previous section to determine magnitudes cannot be directly applied to the study of proper motions. When aligning the catalogues, the proper motion information is effectively averaged out to achieve high-precision magnitudes. Fortunately, the initial stages of the analysis—such as the PSF determination and the measurements for each single filter—are unaffected by this process, allowing the proper motion analysis to start from that point.
The `xym2mat` routine was used to individually align each set of images to the Gaia reference frame. Then, `xym2bar` was applied to combine images taken with the same filter at the same epoch, identifying common stars across them. Consistent with the previous section, the minimum number of images in which a star must be detected to be included in the analysis was set to 1. Finally, using `xym1mat`, the catalogues were matched across different epochs, preparing the data for the proper motion analysis.
The proper motion analysis itself was carried out using a `FORTRAN` routine, `lnk2res`, provided by Anderson et al. (2008). This code computes the coefficients for local transformations using reference stars, selected by the user, to calculate the most accurate displacements relative to these reference stars.

The output of this code provides the displacement δx and δy of each star in the x and y coordinates, relative to the first epoch, along with the root-mean-square errors. To each observation, the corresponding time—recorded as Julian Date (JD)—must be added, as it is fundamental for determining proper motions. Finally, to obtain the proper motion, a linear fit is performed for both δx and δy as a function of JD for each star in the catalogue; this is done assuming a linear motion, so that the slope of the fit represents exactly the proper motion.
It is important to note that a star must be observed at least once in both epochs for the proper motion to be measurable. If a star is detected only in one epoch, even if in multiple images (taken only a few hours apart), the motion of the star remains undetectable due to the short time interval. Finally, since all images were aligned to the Gaia reference frame, the proper motion of each star will be expressed in terms of its components $\mu_\alpha \cos\delta$ and μ_δ. Figure 3.7 shows the proper motion of the stars in the analyzed FoV.

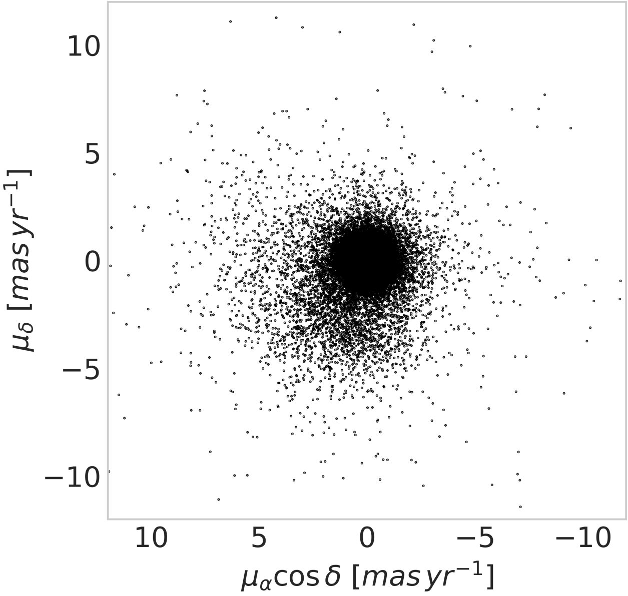

Figure 3.7: Proper motion plot obtained for the Galactic GC NGC 6266.

Chapter 4

Data Analysis

In this chapter, I will analyze the photometric and astrometric catalogues produced so far. The analysis begins with the selection of cluster members using proper motions, followed by applying the proper reddening corrections to the CMD. After these preliminary steps, I will provide an initial examination of the kinematic properties of NGC 6266 by studying its general kinematic behavior. Then, I will use the chromosome map to disentangle between 1P and 2P stars within the cluster. Finally, I will separately analyze the kinematic properties of the two populations.

Before starting the analysis, the first step consists in selecting the cluster members. The FoV contains stars that do not belong to the cluster but are merely projected along the same region of sky. To determine which stars belong to the cluster, I used information derived from proper motions.

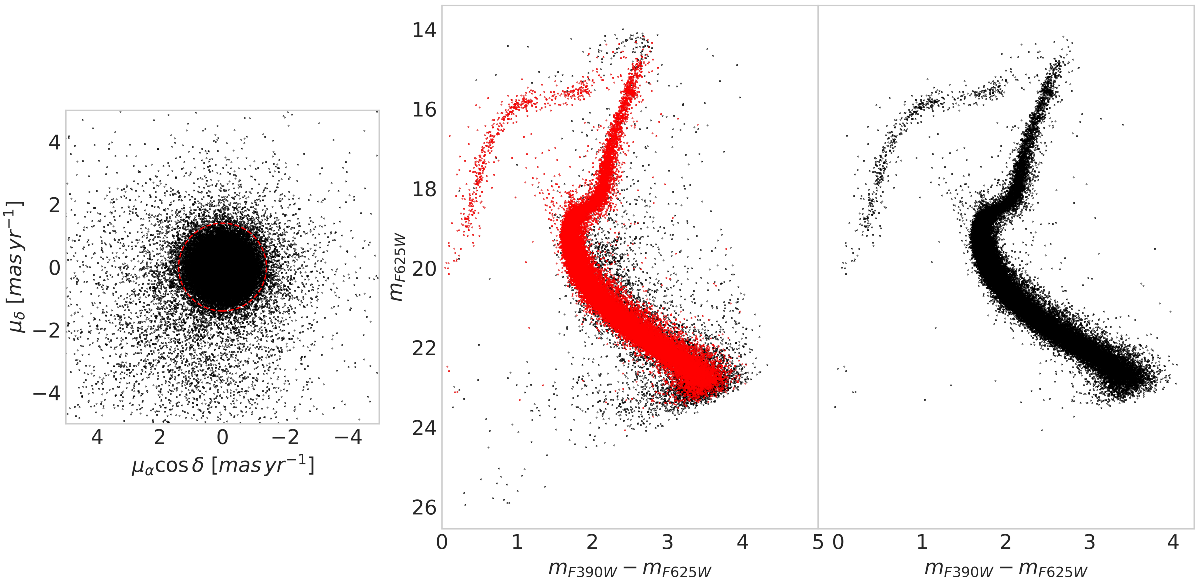

Figure 4.1: Selection procedure for cluster members. The left panel shows the proper motion plot for NGC 6266, with the red circle indicating stars identified as cluster members. The middle panel displays the preliminary CMD of NGC 6266, where red dots highlight the cluster members choosen from the proper motion plot. The right panel shows the final CMD of NGC 6266.

The observations for NGC 6266 were collected over a period of six years (see column 1 in Table 3.1). Using the astrometric catalogue, I generated the left panel of Figure 4.1. The proper motions measured in this way are relative proper motions, meaning they were calculated using a reference frame defined by certain stars within the FoV. As a result, the points in the plot are distributed around the origin at (0, 0). By selecting only the points clustered near the center of the plot, I isolated stars with coherent motion, which are identified as cluster members. These selected members are highlighted in red in the middle panel of Figure 4.1. After removing the field stars, I obtained the final CMD, shown in the right panel of the figure. Although the CMD has been cleaned of field star contamination, we are not yet ready to study multiple populations. We need to correct for differential reddening first. Differential reddening causes a spread in the CMD sequence that must be corrected to accurately observe the intrinsic broadening of the sequence, which indicates the presence of multiple populations.

4.1 Differential Reddening

Light emitted by an astronomical source does not travel unperturbed towards us. The presence of gas and dust clouds along the line of sight dramatically affect photometric measurements. In particular, gas tends to absorb and re-radiate light in different directions, while dust tends to scatter the radiation (Draine, 2003). This effect, known as **extinction**, must be corrected in the photometric catalogue obtained in the previous chapter to ensure accurate results.

Interstellar absorption, is the coefficient that quantifies for this effect. It is defined as the difference between the observed magnitude at a given wavelength, $m(\lambda)$, and the intrinsic magnitude, m_0:

$$A_\lambda = m_\lambda - m_0 \tag{4.1}$$

This coefficient is wavelength dependent. According to Whitford's law, $A_\lambda \propto \lambda^{-1}$, extinction affects more the blue part of the spectrum compared to the red part.

Since we observe in different photometric bands, the difference in interstellar absorption between two bands is referred to as **color excess**:

$$E(\lambda_1 - \lambda_2) = A_{\lambda_1} - A_{\lambda_2} \tag{4.2}$$

Combining this formula with Whitford's law, we understand why this effect is called **reddening**: extinction tends to shift the color of an astronomical source towards the red part of the spectrum.

Finally, the **reddening coefficient** R_λ is defined as the ratio between interstellar absorption and color excess:

$$R_\lambda = \frac{A_\lambda}{E(\lambda_1 - \lambda_2)} \tag{4.3}$$

This ratio is fundamental in deriving the proper corrections for reddening to apply to our data. Once we know R_λ and the color excess, we can determine the interstellar absorption needed to correct our data.

Historically, astronomers estimated a value of $R_V = 3.1$ for the Milky Way. However, we now understand that this value is not universally accurate. For example, in regions like the Galactic bulge, characterized by a high concentration of Interstellar Medium (ISM), different values are more appropriate. In the previous study of NGC 6266, Milone (2015) used this traditional value for reddening corrections. In this work, however, I adopted the updated estimate from Legnardi et al. (2023), who determined that a value of $R_V = 2.7$ better represents the reddening in the direction of the Galactic bulge. This estimate is based on observations of 56 GCs located in that region. The corresponding corrections for the HST filters used in this study are as follows:

F390W	F435W	F625W	F658N
1.344	1.258	0.874	0.772

Table 4.1: Reddening coefficients for HST filters used in this work, derived according to Legnardi et al. (2023). Each value in the table is normalized with respect to $A(V)$.

However, gas and dust may not be homogeneously distributed within the FoV. As a result, interstellar absorption can vary locally within the image (Legnardi et al., 2023). This effect is known as **differential reddening**, and its effect consist in adding additional spread to the sequence in the CMD, which needs to be removed to detect multiple populations.

In this work, I address differential reddening following the method outlined by Milone et al. (2012), which involves three main steps:

1. The first step is to create a new reference frame (see panel a in figure 4.2) based on the original CMD. The differential reddening vector, indicated by the red arrow in the figure, defines the directions of the new $\hat{x}-$axis, referred to as *abscissa* in the original paper. The new *ordinate* axis is orthogonal to it. The origin of this new frame is chosen to create the biggest possible angle between the reddening vector and the main sequence.

2. In the second step, the cluster is rotated until it aligns with the new reference frame (see panel b). After this alignment, a portion of the main sequence is selected, delimited by a two black dotted lines in the figure. Stars within this region are used to derive the fiducial line (dashed red line in the figure). The fiducial line is obtained by dividing the sample of points in square bins of $0.4\,mag$ size, calculating the median abscissa and ordinate for each bin, and then fitting these points together.

3. In the final step, shown in panel c, differential reddening is estimated by measuring the distance between each star and the fiducial line.

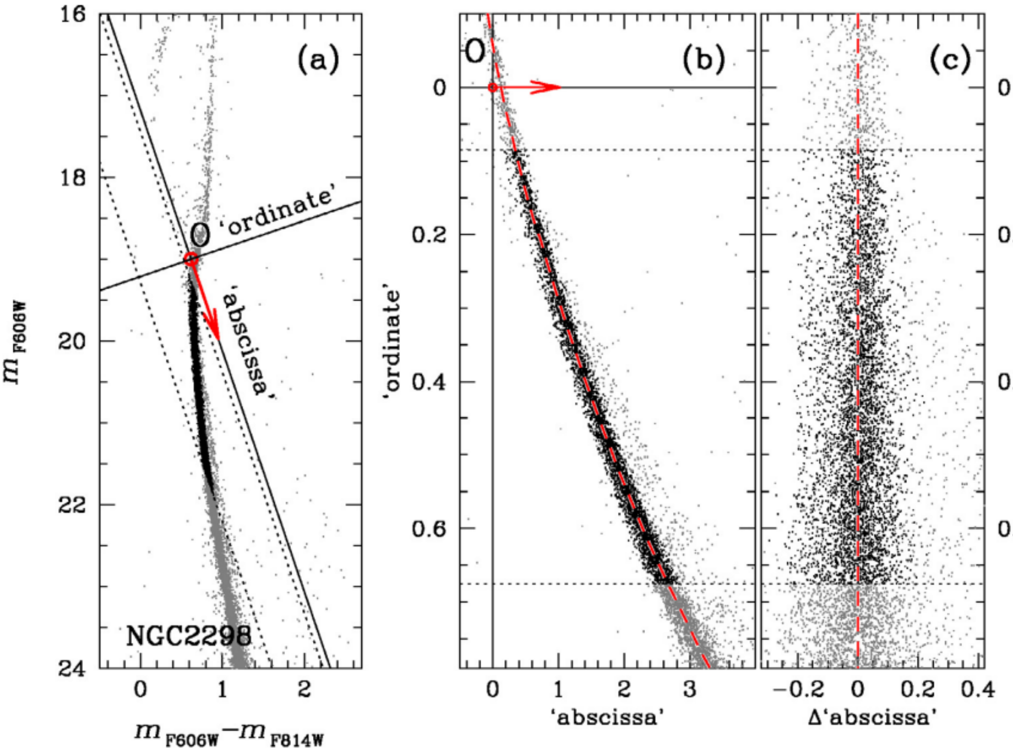

Figure 4.2: Panel a: CMD of NGC 2298, with the red arrow indicating the direction of the reddening vector and the two black continuous lines defining the direction of the new reference axes. Panel b: stars in the new reference frame, with the red dashed line showing the fiducial line of the main sequence. Panel c: *ordinate* vs Δ-*abscissa* diagram used to infer the differential reddening corrections (Milone et al., 2012).

To correct the magnitude of a single star for differential reddening, we calculate the median value of the *abscissa* distance for the nearest stars to the target stars, creating a new sub-sample in the following step. Once the correct CMD is obtained, the procedure is repeated iteratively using the newly derived CMD. This iterative approach significantly improves the estimate of differential reddening.
Figure 4.3 shows the final outcome of this procedure. The left panel displays the original CMD, while the right panel demonstrates the improvement achieved by applying differential reddening corrections. In particular, the turn-off region, where the sequence shrinks significantly, now clearly shows the true broadening effect, which is a reliable indicator of the presence of multiple populations.

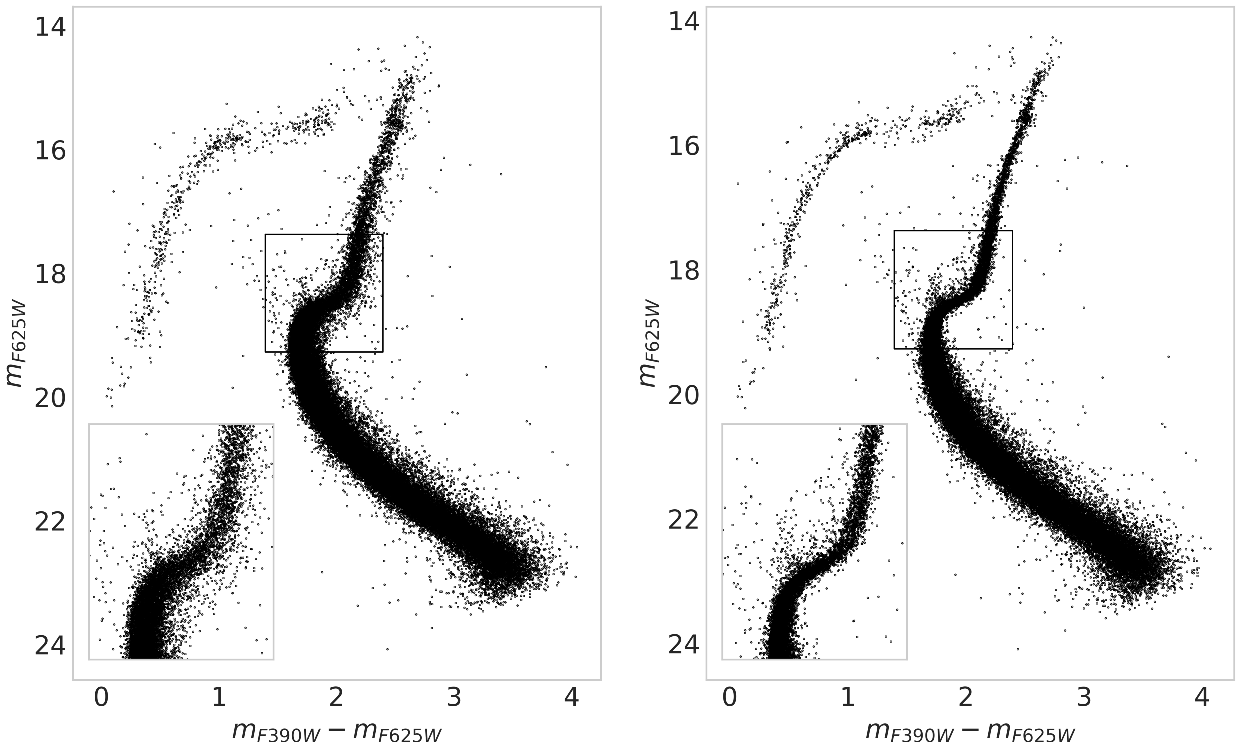

Figure 4.3: The images show how the differential reddening corrections applied to NGC 6266 significantly reduce the spread of the sequence. The CMD on the left has no correction, while the onw on the right has been corrected for differential reddening. Corrections are particularly evident in the turn-off region, highlighted by the two boxes in the plots.

4.2 Kinematic Analysis of NGC 6266

The first step of the analysis involves projecting the components of the proper motion vector ($\mu_\alpha \cos\delta$, μ_δ), which are aligned with the Gaia reference frame as explained in the previous chapter, into radial and tangential components for each star. This projection is illustrated in Figure 4.4. As depicted, the radial component is defined as the apparent motion of the star projected along the line connecting the center of the cluster and the star, while the tangential component is orthogonal to this line.

The reason for performing these projection operations is that this representation of the proper motion vector in polar coordinates reveals interesting properties related to the kinematics of stars in the cluster (Milone et al., 2018b; Libralato et al., 2022).

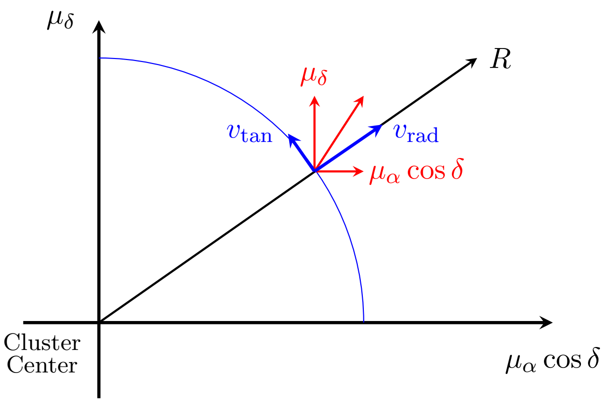

Figure 4.4: Schematic representation of the projection operation of the components of the proper motions. The red arrows represent the proper motion components in the original Gaia frame, while the blue arrows show the projected components along the radial and tangential directions relative to the cluster center.

However, before proceeding, I need to identify the center of the cluster. Although this may seem straightforward, it presents several challenges.
First, a simple approach of finding the point of highest density in the spatial distribution of the cluster is not effective. This is because, as discussed in Chapter 4, the central region of the cluster is poorly measured due to the high concentration of stars, which makes it difficult to build a reliable PSF model. Additionally, the cluster image (see Figure 4.5) is not symmetric; the cluster's center is located towards the right side of the image, which biases any attempt of identify the cluster center in this way.
One algorithm that addresses this issue is proposed by Cordoni et al. (2020). It fits elliptical curves to the isodensity contours of the star distribution in the cluster. Unfortunately, I was unable to implement this technique due to having only a partial image of the cluster.
My solution involves using a clustering algorithm called **KMeans** (Pedregosa et al., 2011), developed in Python, to identify the clustering properties of the star distribution and thus locate its center. It is important to note that I applied the algorithm only to the right side of the figure, as it performs better for identifying spherical cluster regions. After running the algorithm, I determined the center of the cluster to be at the coordinates (6606, 4937) pixels.

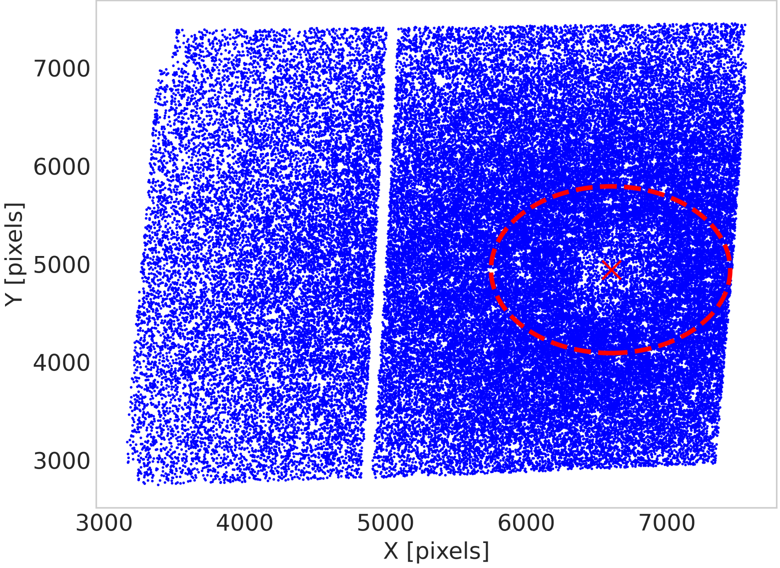

Figure 4.5: Procedure for identifying the cluster center. Blue dots represent the stars in the cluster, the red circle identifies the cluster region used by the algorithm, and the red cross marks the position of the cluster center.

Once the position of the cluster center has been identified, we can use the following equations to project form GAIA frame to polar coordinates

$$V_{rad} = \frac{X \cdot \mu_\alpha \cos\delta + Y \cdot \mu_\delta}{R} \qquad V_{tan} = \frac{Y \cdot \mu_\alpha \cos\delta - X \cdot \mu_\delta}{R}$$

Where (X, Y) represents the position of the star in the reference frame in which the center of the cluster coincides with the origin of the reference frame. $(\mu_\alpha \cos\delta, \mu\delta)$ are the components of the proper motions vector for each star. Finally R represents the distance between the each star and the center of the cluster. The choice of signs in the two equations defines a clockwise orientation for positive values of V_{tan}, while V_{rad} is considered positive when pointing outward.

4.2.1 Velocity Dispersion profiles

Now that the proper motion components have been moved to polar coordinates, is possible to identify the intrinsic velocity dispersion of the stars and study their kinematics.
In order to derive the velocity dispersion of the stars, I followed the procedure described by Mackey et al. (2012) and Cordoni et al. (2020). This procedure consists in a parameter estimation problem,

based on the minimization of a Likelihood $\mathcal{L}(\vec{\theta}\,|\,\vec{d})$ which describes the probability of finding a star with a given **velocity** and a given **intrinsic velocity dispersion**, noted as σ_p in the following discussion. However, let's be a bit more precise about this. The starting point to obtain an estimate for σ_p is the Bayes theorem, which schematically can be written as[1]:

$$\text{prob}(\text{parameters}\,|\,\text{data},\, I) = \frac{\text{prob}(\text{data}\,|\,\text{parameters},\, I) \times \text{prob}(\text{parameters}\,|\,I)}{\text{prob}(\text{data}\,|\,I)} \tag{4.4}$$

Let's now analyze the expression term by term in the context of parameter estimation:

- **prob(data | parameters**, I): this term is called the Likelihood and to derive it, I follow the idea of Walker et al. (2006) who assumed that multiple measurements of a certain star, with true velocity μ follow a Gaussian distribution with mean $\langle\mu\rangle$ and variance σ^2. However this variance is given by the sum of two contributes the random internal measurement uncertainty σ^2 and the **intrinsic radial velocity dispersion** σ_p^2. The latter is the physical quantity we are interested to measure in order to study the kinematic behaviour of the stars in the cluster. Therefore, we can write the joint probability function as the product of the individual Gaussian probabilities for each of the N stars that compose our sample as:

$$\mathcal{L}(\{v_1, \dots,\, v_N\}\,|\,\sigma_p,\, \langle\mu\rangle) = \prod_{i=1}^{N} \frac{1}{\sqrt{2\pi(\sigma_i^2 + \sigma_p^2)}} \exp\left[-\frac{1}{2}\frac{(v_i - \langle\mu\rangle)^2}{\sigma_i^2 + \sigma_p^2}\right] \tag{4.5}$$

- **prob(parameters** | I): this term is called Prior, it describes our initial degree of belief before performing the experiment or looking to the data; in order to be as much uninformative as possible I decided to consider a **uniform prior**.

- **prob(parameters | data**, I): This term is called Bayesian posterior, and it represents the updated belief about an uncertain parameter after observing data.

- **prob(data** | I): actually, the calculation of the full posterior probability would require also the knowledge of the Bayesian evidence. However, since the evidence does not depend on the parameters, and here we are interested in a parameter estimation problem, it just plays the role of an irrelevant normalization factor, therefore from now on we can just omit it.

Therefore, selecting a uniform prior and omitting the Bayesian evidence, in the context of parameter estimation the posterior probability is reduced to the study of the Likelihood function, equation 4.6

$$P(\sigma_p,\, \langle\mu\rangle\ |\, \{v_1,\, \dots,\, v_N\}) \propto \mathcal{L}(\{v_1, \dots,\, v_N\}\,|\,\sigma_p,\, \langle\mu\rangle) \tag{4.6}$$

Moreover, since the logarithm is a monotonically increasing function of its argument, the maximization of the logarithm of a function is equivalent to the maximization of the function itself. We can therefore study the logarithm of the posterior probability, which can be written in a easier way using simple

---

[1] In this general notation, I refers to a general background information.

mathematical tricks:

$$\begin{aligned}
\log P(\sigma_p,\, \langle\mu\rangle \mid \{v_1,\, \dots,\, v_N\}) &= \log \mathcal{L}(\{v_1, \dots,\, v_N\} \mid \sigma_p,\, \langle\mu\rangle) \\
&= \log \left(\prod_{i=1}^{N} \frac{1}{\sqrt{2\pi(\sigma_i^2 + \sigma_p^2)}} \exp\left[-\frac{1}{2} \frac{(v_i - \langle\mu\rangle)^2}{\sigma_i^2 + \sigma_p^2} \right] \right) \\
&= \sum_{i=1}^{N} \log \left(\frac{1}{\sqrt{2\pi(\sigma_i^2 + \sigma_p^2)}} \exp\left[-\frac{1}{2} \frac{(v_i - \langle\mu\rangle)^2}{\sigma_i^2 + \sigma_p^2} \right] \right) \\
&= \sum_{i=1}^{N} \left(\log \left[\frac{1}{\sqrt{2\pi(\sigma_i^2 + \sigma_p^2)}} \right] + \log \left[\exp \left(-\frac{1}{2} \frac{(v_i - \langle\mu\rangle)^2}{\sigma_i^2 + \sigma_p^2} \right) \right] \right) \\
&= \sum_{i=1}^{N} \left[-\frac{1}{2} \log 2\pi(\sigma_i^2 + \sigma_p^2) - \frac{1}{2} \frac{(v_i - \langle\mu\rangle)^2}{\sigma_i^2 + \sigma_p^2} \right] \\
&= -\frac{1}{2} \sum_{i=1}^{N} \left[\log 2\pi(\sigma_i^2 + \sigma_p^2) + \frac{(v_i - \langle\mu\rangle)^2}{\sigma_i^2 + \sigma_p^2} \right]
\end{aligned}$$

The expression I obtain above is valid for a single component of the velocity, but as I said at the beginning of the section, I'm considering both radial and tangential velocity components, to take into account this effect in the posterior probability, I did the reasonable assumption of considering the measurement of the two components to be independent. In this way we can avoid to consider correlation terms, and the joint log-probability becomes the sum of the log-probabilities relative to the two components

$$\log P(\vec{\theta} \mid \vec{d}) = \log P(\vec{\theta}_r \mid \vec{d}_r) + \log P(\vec{\theta}_t \mid \vec{d}_t) \tag{4.7}$$

where I introduce a new notation to simplify the formula. In this new notation $\vec{\theta}$ is used to indicate the vector of parameters, while $\vec{d}$ is used to indicate the vector of data. To be more precise, we have that:

1. $\vec{\theta}_r = (\sigma_r,\, \langle\mu_r\rangle)$
2. $\vec{d}_r = (\{v_{r1},\, \dots,\, v_{rN}\})$
3. $\vec{\theta}_t = (\sigma_t,\, \langle\mu_t\rangle)$
4. $\vec{d}_t = (\{v_{t1},\, \dots,\, v_{tN}\})$
5. $\vec{\theta} = (\sigma_r,\, \sigma_t,\, \langle\mu_r\rangle,\, \langle\mu_t\rangle)$
6. $\vec{d} = (\{v_{r1},\, \dots,\, v_{rN},\, v_{t1},\, \dots,\, v_{tN}\})$

The meaning of each term is explained in table 4.2.

Parameter	Meaning
σ_r	Intrinsic radial velocity dispersion
σ_t	Intrinsic tangential velocity dispersion
$\langle\mu_r\rangle$	Mean radial velocity
$\langle\mu_t\rangle$	Mean tangential velocity
v_{ri}	Radial velocity of the i^{th} star
v_{ti}	Tangential velocity of the i^{th} star

Table 4.2: Meaning of each parameter of the Likelihood function.

Finally, the overall log-posterior probability can be written as

$$\log P(\vec{\theta} \mid \vec{d}) = -\frac{1}{2} \sum_{i=1}^{N} \left[\log 2\pi(\sigma_{er,\,i}^2 + \sigma_r^2) + \frac{(v_{r,\,i} - \langle\mu_r\rangle)^2}{\sigma_{er,\,i}^2 + \sigma_r^2} + \log 2\pi(\sigma_{et,\,i}^2 + \sigma_r^2) + \frac{(v_{t,\,i} - \langle\mu_t\rangle)^2}{\sigma_{et,\,i}^2 + \sigma_t^2} \right] \tag{4.8}$$

Then, in order to derive the best estimates for the parameters I used a Markov Chain Monte Carlo (MCMC) algorithm (Metropolis et al., 1953), with the aims of maximizing the posterior probability (4.8).
The idea behind the Monte Carlo approach is to handle a posterior distribution that is analytically intractable by drawing random samples from it and numerically averaging over them to compute quantities of interest (Sivia and Skilling, 2006). By generating these random samples, we aim to find the optimal value of the parameter vector $\vec{\theta}$. The parameters are treated as random variables, assumed to be distributed according to the posterior probability distribution.
Since directly sampling from the posterior is not always feasible, we employ a MCMC method, which generates a sequence of samples from a probability distribution by constructing a Markov Chain. This chain, once sufficiently sampled, converges to the posterior distribution, allowing us to approximate the desired quantities.
Concretely, the MCMC process works as follows:

1. **Initialization**: We begin by choosing an arbitrary starting point for the parameter vector $\vec{\theta}_0$ within the parameter space. This starting point does not need to be drawn from the posterior distribution, but it should be within a reasonable range based on prior knowledge.

2. **Transition mechanism**: At each step of the chain, the algorithm proposes a new candidate value for the parameter vector, say $\vec{\theta}_{\text{new}}$, based on the current value $\vec{\theta}_{\text{current}}$. The new value is proposed according to a transition probability that depends on the specific MCMC method used.

3. **Acceptance step**: Once a new candidate is proposed, the algorithm decides whether to accept or reject it. This decision is probabilistic and ensures that, over time, the chain will converge to the target distribution.

4. **Iterative sampling**: This process of proposing and accepting or rejecting new samples is repeated for a large number of steps. Initially, the chain may take some time to *warm up* and converge to the posterior distribution. This early phase is called the burn-in period, and the samples generated during this phase are discarded.

5. **Convergence**: After the burn-in period, the chain will begin to sample values that are representative of the posterior distribution. At this stage, every step in the chain is considered a valid sample from the posterior, and the more samples collected, the better the approximation of the distribution.

To implement this approach I use `emcee` (Foreman-Mackey et al., 2013), an MCMC algorithm written in `python`, which has the main advantage, compared to traditional MCMC methods of employing multiple *walkers*, which are nothing else than parallel chains, that explore the parameter space simultaneously. Each of these walkers is an independent Markov Chain; the reason for using this multiple chain approach is to avoid of falling into local minima in the parameter space improving significantly the convergence of the posterior.

Finally, to set up the MCMC, I decided to divide the stars in the cluster into radial bins, starting from the center of the cluster. Each bin contains the same number of stars, which means that the innermost bins are smaller than the outer ones due to the decreasing density of stars as we move outward. After defining these bins, I passed them to my algorithm, which minimizes the log-likelihood (see equation 4.8 to find the intrinsic velocity dispersion for the stars within each bin.
The resulting velocity dispersion values are then combined with the radial distance of each bin from the center of the cluster to derive the velocity dispersion profile. This process will be repeated three times: first for the entire cluster to analyze the overall kinematics, then separately for the main sequence and the red-giant branch stars. In these latter cases, I will use the ChM to disentangle the different populations within NGC 6266 and study their kinematics individually.
All analyses were conducted in `python`, utilizing widely used libraries such as `numpy` for numerical operations (Harris et al., 2020), `matplotlib` for data visualization (Hunter, 2007), `scipy` for scientific computing (Virtanen et al., 2020), `pandas` for data manipulation (Wes McKinney, 2010; pandas de-

velopment team, 2020), and `pygtc` for corner plot generation (Bocquet and Carter, 2016). Finally, to run the MCMC I choose the following set of parameters:

Parameters	Walkers	Steps	Burn-In	Thinning
Value	35	10000	2500	100

Table 4.3: Values of the parameters used for the MCMC analysis.

4.2.2 Overall Kinematics

Having described the procedure to obtain the intrinsic velocity dispersion of the components for stars in the Galactic GC NGC 6266, I now need to select the optimal sample of stars to which I can apply this technique to estimate the velocity dispersions. Ideally, intrinsic velocity dispersion is a fundamental property of all stars, so using all stars in my CMD would provide the most comprehensive velocity dispersion plots. However, this is not practically feasible.

Fainter stars have been observed over fewer epochs compared to brighter stars. Additionally, their faintness leads to larger intrinsic positional uncertainties in the PSF model compared to brighter stars. A similar limitation applies to very bright stars, which can saturate the CCD and produce less reliable measurements.

I identified the optimal interval for investigation as between 17 and 21 magnitudes, which exhibit a roughly constant intrinsic dispersion. After identifying this magnitude range, I proceeded with the overall analysis of the cluster. At this stage, I did not consider the two populations separately; instead, I studied all the stars in the cluster within the defined magnitude interval.

I applied the MCMC procedure described in section 4.2.1, obtaining the plots shown in Figure 4.7. To verify whether the Markov Chain converges correctly to a stationary probability distribution and whether the chosen burn-in value was appropriate, I performed a **Gelman-Rubin test**. This test involves running several chains and computing averages and variances for the parameters separately using samples from each chain. Then, I calculated the variance of the average values extracted from each chain. If there is good convergence and mixing, the averages from each chain will be similar, and the variance between these averages will be much smaller than the variance of the parameter itself. The Gelman-Rubin statistic is defined by the following ratio:

$$\hat{R} = \frac{\hat{V}}{W} \tag{4.9}$$

where $\hat{V}$ is the statistical estimator for the variance of a parameter defined as

$$\hat{V} = \frac{n-1}{n}W + \frac{B}{n} \tag{4.10}$$

In this equation, the first term on the right-hand side represents the variance computed within a chain, averaged over all chains, while the second term is the variance between the chains. If the ratio in equation (4.9) tends toward 1, we achieve good mixing and convergence of the chains; otherwise, the convergence is poor.

The analysis of the overall kinematics of the cluster, reported in figure 4.7, passes the test.

The first two plots at the top of the figure show the radial and tangential velocity dispersion profiles for the cluster, estimated as a function of radial distance from the cluster center. The horizontal error bars in the plots indicate the range of the radial bins. Additionally, the core radius and half-light radius of NGC 6266 are marked, with values obtained from (Baumgardt and Hilker, 2018). These radii are included because they help infer general characteristics of cluster behavior, allowing for comparisons with other clusters.

In the case of NGC 6266, the plots display the typical pattern observed in stellar clusters: velocity dispersions are higher near the cluster core due to the greater density of stars and the increased gravitational interactions. These interactions result in a higher velocity dispersion for stars in this region. As the distance from the cluster center increases, the dispersion profile decreases, reflecting

the lower stellar density and reduced gravitational interactions.
The two middle plots in figure 4.7 illustrate the mean velocity behavior of stars in both the radial and tangential components. Both plots show average velocities that are consistent with zero, which may indicate that the cluster is in a state of dynamical equilibrium, with stars moving without a preferred direction.
This observation aligns with the analysis shown in the bottom plot of figure 4.7, often referred to as the **anisotropy plot**. In this plot, the x-axis represents the radial distance from the cluster center, as in the previous plots, while the y-axis represents the anisotropy factor, defined as follows:

$$\text{Anisotropy} = \frac{\sigma_{tan}}{\sigma_{rad}} - 1 \tag{4.11}$$

This plot is valuable for identifying any preferential direction of stellar motion within the cluster. According to equation (4.11), a positive anisotropy coefficient indicates tangential anisotropy, implying that orbits are predominantly circular. Conversely, a negative coefficient suggests radial anisotropy, where stars tend to have radial orbits, moving either toward or away from the cluster center.

This plot was introduced in the context of multiple populations to help infer kinematic differences among them. According to the work of Vesperini et al. (2021), simulations that assume a higher central density of 2P stars relative to 1P stars in clusters that are not dynamically evolved indicate that 2P stars tend to develop radial anisotropy, while 1P stars remain largely isotropic. Figure 4.6 illustrates the expected behavior for multiple populations under this model.
In dynamically older clusters, prolonged interactions between stars can erase these kinematic signals over time, making it harder to detect any initial differences in anisotropy.

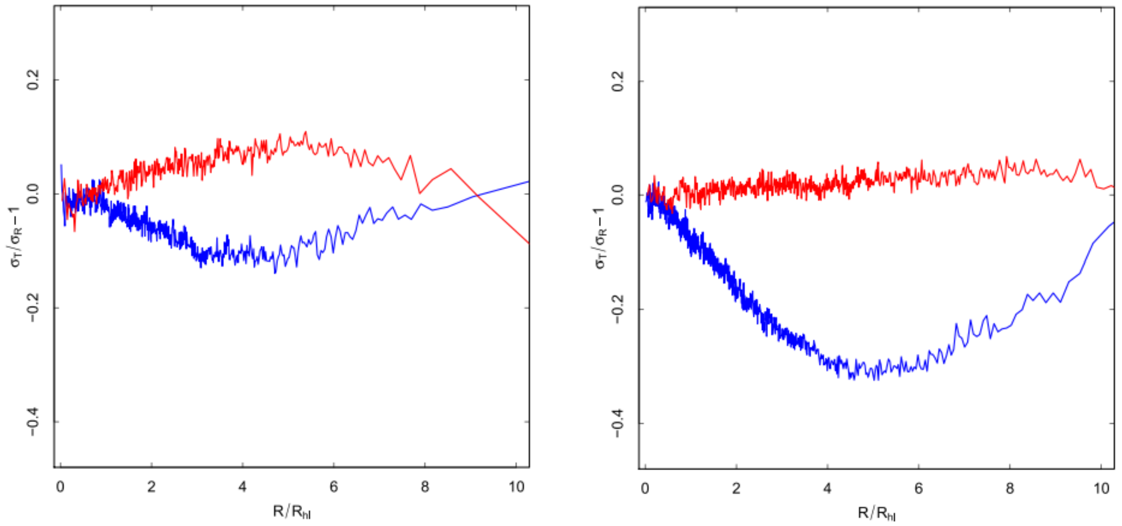

Figure 4.6: Radial profile of the velocity anisotropy for 2P (blue) and 1P (red) in two different simulated clusters at $t = 12, Gyr$, as per Vesperini et al. (2021). The left simulation assumes a mass ratio of $M_{2P}/M_{tot} = 0.80$, while the right simulation assumes $M_{2P}/M_{tot} = 0.77$.

In this analysis, I applied the technique to the entire cluster population without distinguishing between the two subpopulations, aiming to assess the general kinematic behavior of NGC 6266. The global kinematic analysis detected no evidence of anisotropy, suggesting that this cluster is in an isotropic state.

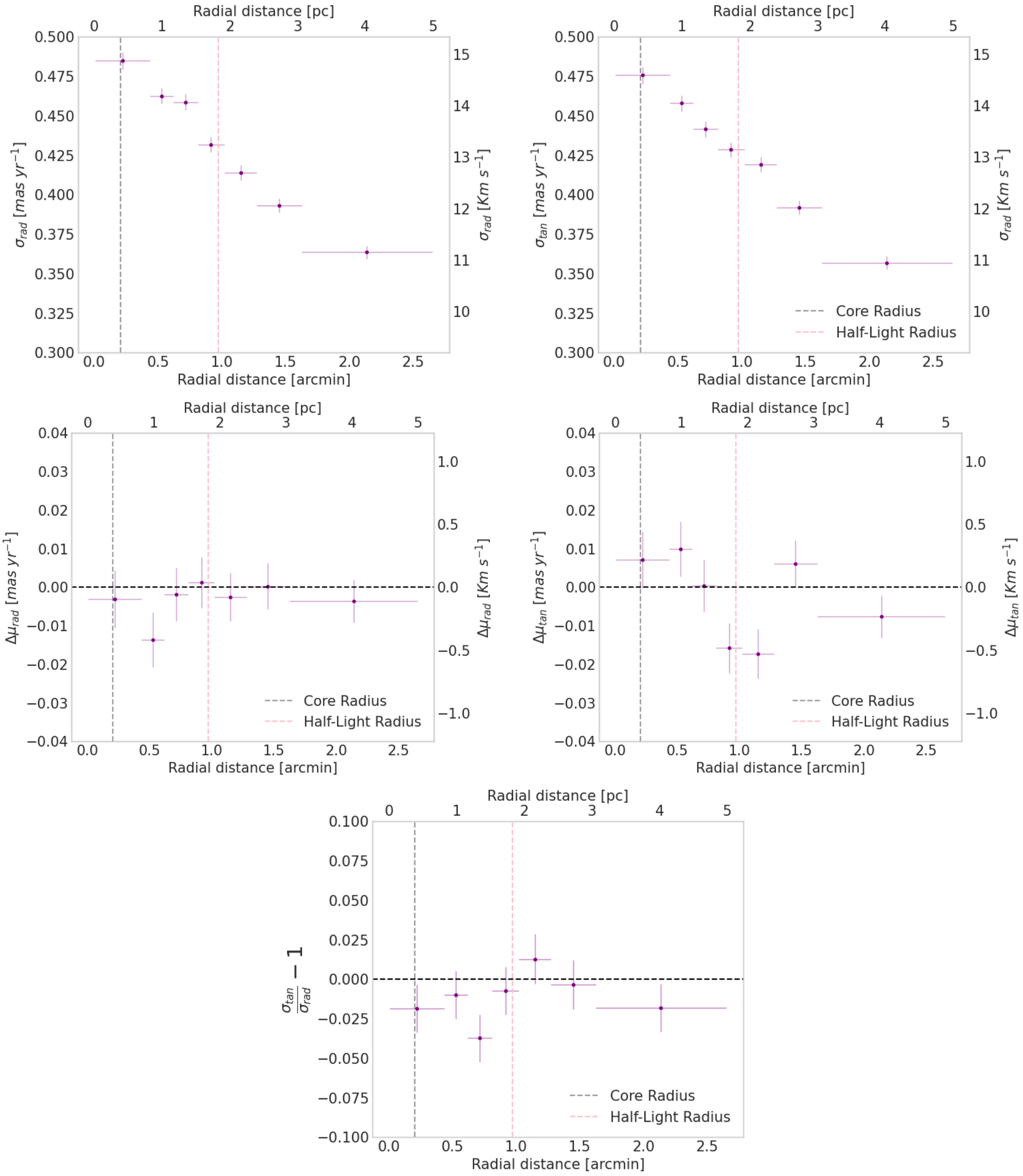

Figure 4.7: Overall Kinematics of NGC 6266. The two upper plots show the average tangential and radial motions of the stars in the cluster as a function of the radial distance from the cluster center. The two middle plots show the velocity–dispersion profiles for the radial and tangential velocity components. Finally the bottom plot shows the anisotropy profile of the cluster. The horizontal errorbars, mark the extension of the radial bins, while the black and pink dashed lines indicate the core and the half-light radius, respectively, and their values have been taken from Baumgardt and Hilker (2018).

4.2.3 Main Sequence Kinematics

Once the global analysis has been done, its time to move to the analysis of the individual stellar populations of NGC 6266. To do that, I focused my analysis in two precise regions of the CMD: the upper Main Sequence (MS) and the RGB. The reason why I select these two regions is that usually they are good candidates to identify the presence of multiple populations, based on the intrinsic broadening of the sequence. Other regions, such as the turn off cannot be used to this purpose since, according to simulations and stellar model, the sequences of multiple populations tends to merge there. Then I analyze individually each of them, using a similar approach to the one used by Milone (2015) to split the two extreme populations of this cluster. I improve this previous work, extending this analysis also to the RGB and deriving the first chromosome map for this cluster.

As already discussed in chapter 1, the breakthrough discovery in the field of GCs was the discovery of the phenomena of multiple populations. Milone et al. (2015) introduced the ChM as a fundamental tool to distinguish the different stellar population based on a photometric approach.
In order to obtain the first ChM; for NGC 6266 i followed the following steps:

1. I decided to not consider stars with a radial distance smaller than 50 *arcsec*, which corresponds roughly to 1250 pixels, from the cluster center, in order to avoid the most crowded region. Removing these stars we can clearly see that the MS starts to show a bimodal distribution, with stars that tends to be distributed along two sequences, as shown in figure 4.8.

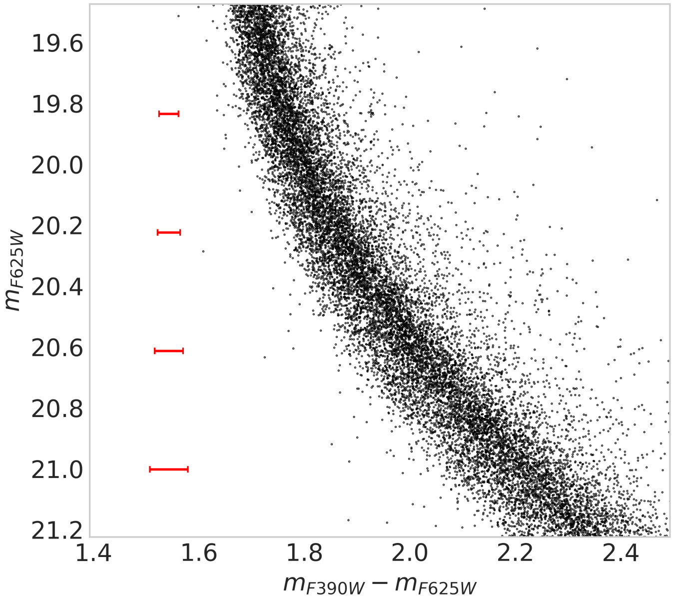

Figure 4.8: Focus on the MS of NGC 6266, after removing stars in the innermost region of the cluster, the main sequence exhibits a bimodal sequence. The photometric errors, shown in red in the plot confirms that the broadening of the sequence has an intrinsic nature.

2. Once I verified that the hint of the double sequence visible in the CMD is an intrinsic one and not due to photometric broadening, I proceed with the *verticalization* process. It consists in cutting the candidate region of the main sequence in a series of horizontal slices, then for each of them sort the array of data and calculate the 4^{th} and the 96^{th} percentile of the distribution. The points obtained are then plotted and joined together generating what is called a fiducial lines. These two lines, red for the 96^{th} percentile and blue for the 4^{th} percentile are shown in figure 4.9. This procedure needs to be done for two different CMDs, built with a different choice of filters, because in order to obtain the ChM we need to combine them. About my candidate cluster, there are only four filters available, so after some attempt, I found that the best CMD to investigate multiple populations have colors $m_{F390W} - m_{F625W}$ and $m_{F435W} - m_{F658N}$, both plotted against m_{F625W}.

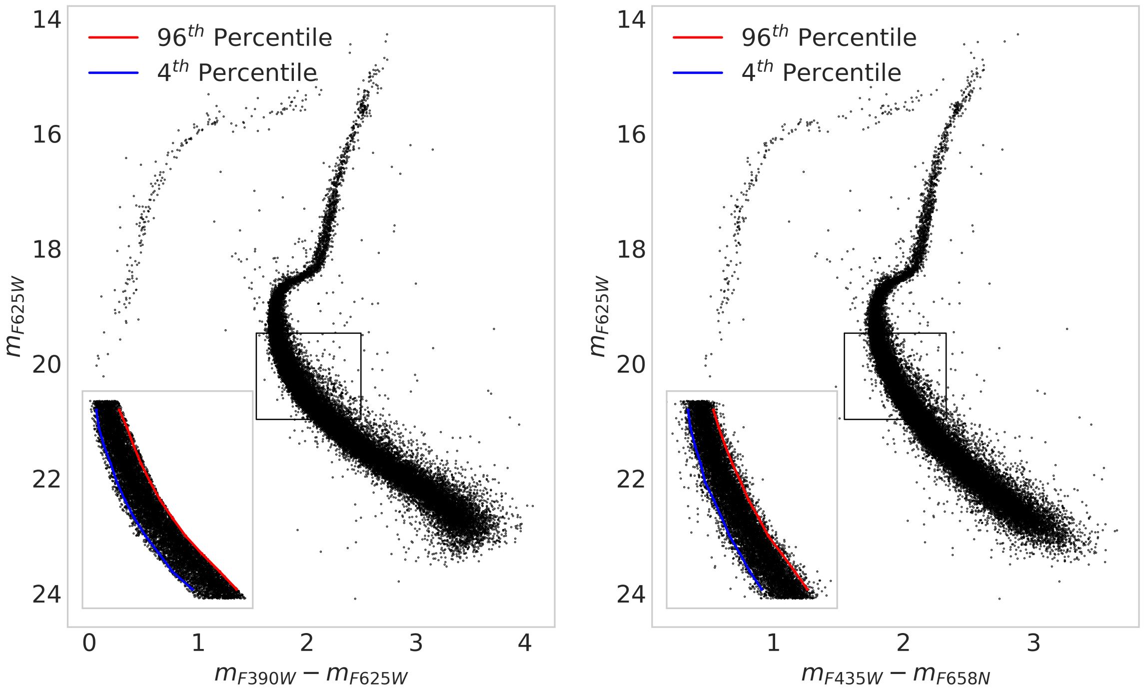

Figure 4.9: Verticalization process for both CMDs of NGC 6266. First one built using $m_{F390W} - m_{F625W}$ color, while the second one obtained from $m_{F435W} - m_{F658N}$ color. The 4th and 96th percentile are drawn, respectively, as the red and blue fiducial lines. The black box in the figure highlights the region of the CMD investigated in this study.

Once I derived the red and blue fiducial lines, I used equations 4.12 and 4.13 to verticalize the CMD, calculating the the so called *Delta* quantity Δ, which represents distance between the color and the blue fiducial line.

$$\Delta_{F390W,\,F625W} = \frac{X - X_{\text{blue fiducial}}}{X_{\text{red fiducial}} - X_{\text{blue fiducial}}} \tag{4.12}$$

$$\Delta_{F435W,\,F658N} = \frac{Y - Y_{\text{blue fiducial}}}{Y_{\text{red fiducial}} - Y_{\text{blue fiducial}}} \tag{4.13}$$

The quantities X and Y in the formulas are related respectively to the colors $m_{F390W} - m_{F625W}$ and $m_{F435W} - m_{F658N}$; while the other parameters are the colors of the red and blue fiducial lines for the two plots.

3. Now that both CMDs have been verticalized, I can proceed with the identification of the multiple populations. In order to do that I plot the two Δ quantities one against the other, obtaining the first ChM of NGC6266, visible in figure 4.10.
   Unfortunately, the filters available on the HST archive for this cluster are not ideal for the study of multiple populations. In fact, F435W, F625W and F658N cover more or less the same portion of the spectra, making difficult to disentangle properly the two populations from the ChM. This is well visible in the left panel of figure 4.10, there is no separation between the two populations as we saw in the plots of figure 1.4. The reason behind this is that the filters collected during the first epoch of observation were collected well before the discovery of multiple populations in GCs and so not with this purpose.

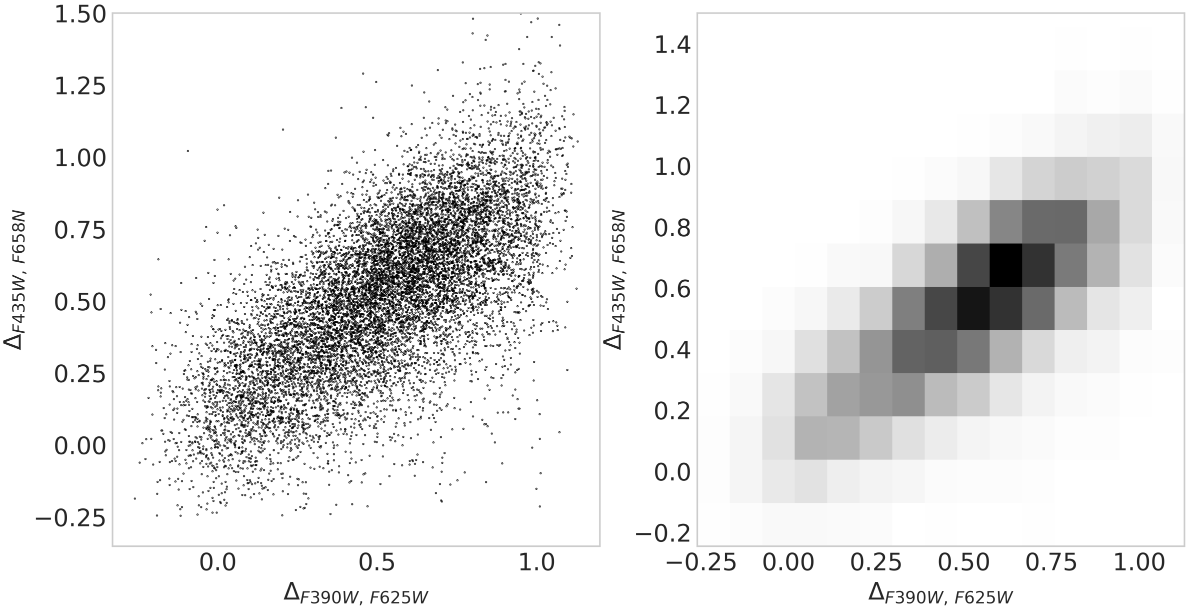

Figure 4.10: On the left panel is shown the ChM of NGC 6266, built using the two colors $\Delta_{F390W,\,F625W}$ and $\Delta_{F435W,\,F658N}$. On the right panel is shown the bi-dimensional histogram representation of the ChM. Even if neither one of them is able to clearly disentangle the populations, both plot shows the presence of a bimodal trend.

According to what I showed so far, it is not possible to separate clearly the two populations of NGC 6266 from the ChM. Therefore I need to find a proper criteria to separate them. My solution to this problem consist in realizing an histogram of $\Delta_{F390W,\,F625W}$, which is visible in the right panel of figure 4.11, where we can clearly notice the presence of two peaks in the distribution. They correspond to the two populations of the cluster. I identified the color corresponding to the valley in between the two peaks, which is marked with a vertical grey line in the plot, and then i used this information to separate the two populations in the ChM, which is now shown in figure 4.12.

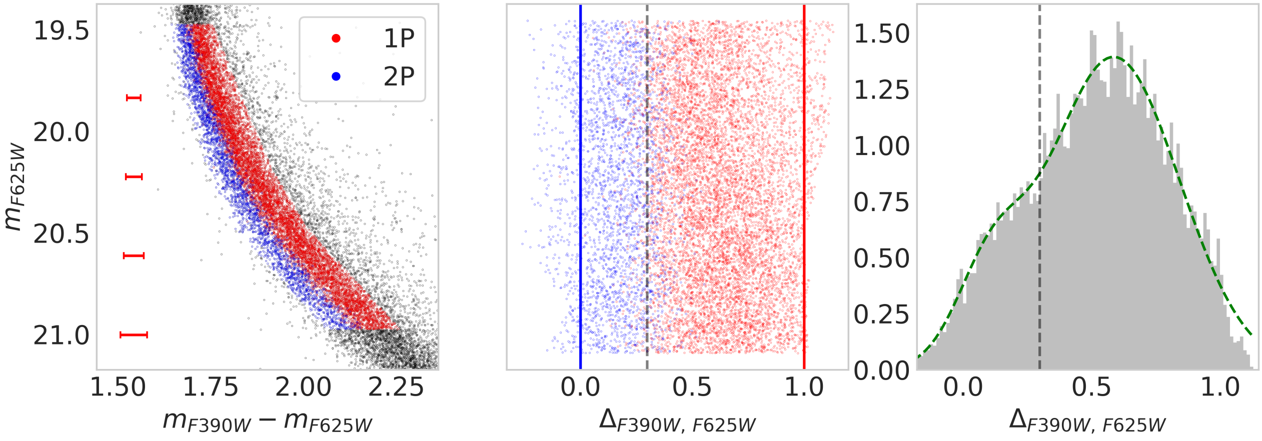

Figure 4.11: The figure shows the procedure to select 1P and 2P stars in the MS of NGC 6266. Left panel: it shows the $m_{F390W} - m_{F625W}$ vs m_{F625W} diagram for the main sequence of the cluster. The red horizontal bars represents the photometric error. Middle panel: it shows the verticalized $m_{F390W} - m_{F625W}$ vs m_{F625W} diagram for the same portion of the MS as the left panel. Blue and red vertical lines represents respectively the $4-th$ and the $96-th$ percentile of the distribution, and highlight the boundaries of the MS. Right panel: it shows the $\Delta_{F390W,\,F625W}$ histogram distribution. The dashed grey vertical line is used to separate the two populations, while the dashed green line, superimposed to the histogram, represents a bimodal Gaussian distribution used to fit the data. In both, left and middle plots, red dots corresponds to 1P stars, while blue dots to 2P stars.

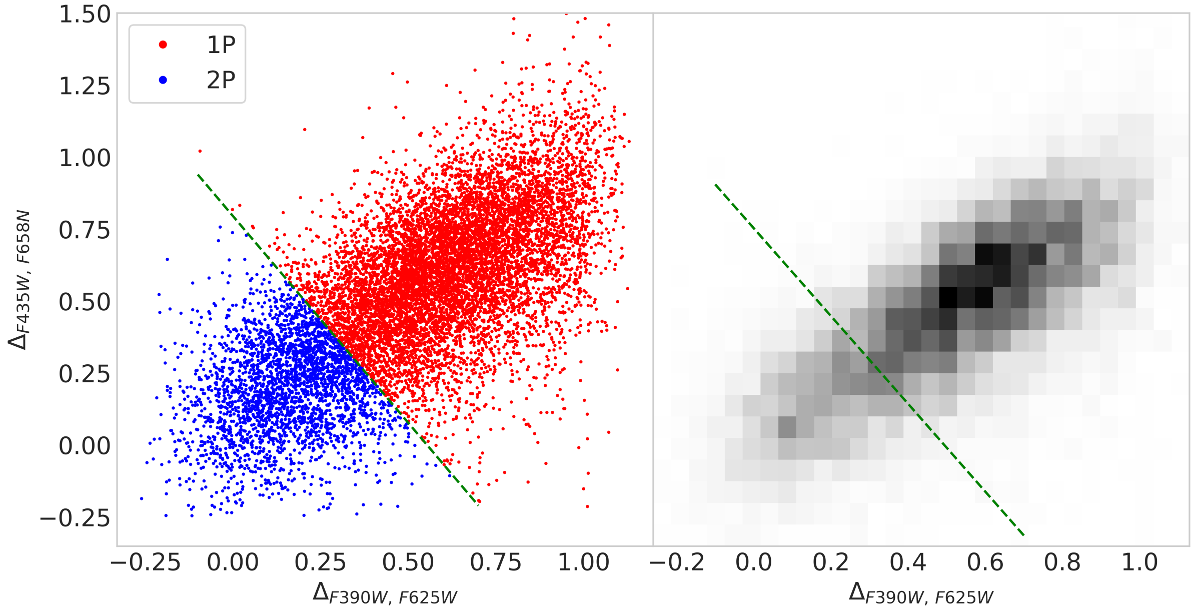

Figure 4.12: Same plots of figure 4.10 but now red and blue dots in the ChM of NGC 6266 represents respectively the first and second populations of the cluster.

The two populations identified in this way correspond to the extreme populations identified by Milone (2015). Milone classified the red MS—which I refer to as 1P—as a stellar population with a primordial level of helium, characterized by high oxygen and low nitrogen content. In contrast, the blue MS, which I label 2P, aligns with a stellar population enhanced in helium but low in oxygen and rich in nitrogen.

In terms of kinematics, I conducted the same analysis as before, this time treating 1P and 2P stars separately. The results are shown in the plots in Figure 4.13, where each simulation successfully passed the Gelman-Rubin test, confirming good convergence and mixing of the chains.
As observed previously in the global kinematic analysis, the cluster exhibits isotropic behavior, even when considering MS stars alone. Both populations show the same kinematic pattern in both the radial and tangential components, with an anisotropy coefficient value close to zero.
However, it is important to note that some 1P stars may have been included in the 2P sample, and vice versa, in varying proportions. This contamination affects the average kinematics of each population and should be taken into account when interpreting the results.

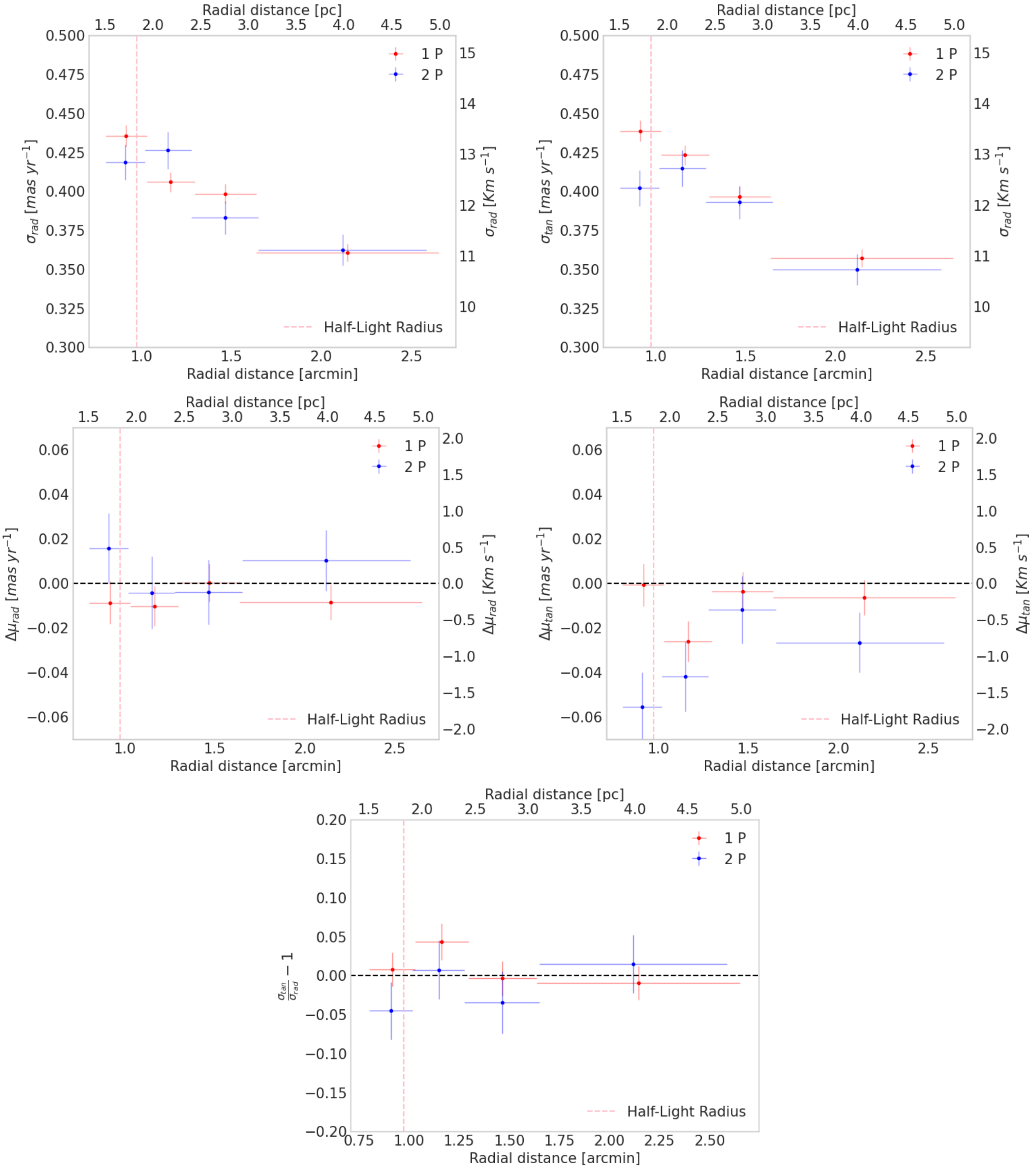

Figure 4.13: Kinematics of MS stars of NGC 6266. The two upper plots show the average tangential and radial motions of 1P stars (red) and 2P stars (blue) as a function of the radial distance from the cluster center. The two middle plots show the velocity–dispersion profiles for the radial and tangential velocity components of the two stellar populations as a function of the radial distance from the cluster center. The bottom plot shows the anisotropy profile of the two populations. The horizontal errorbars, mark the extension of the radial bins. Since in this case I do not considered stars within a radial distance of 1200 pixels from the cluster center, only the half-light radius (pink dashed line), whose value has been taken from Baumgardt and Hilker (2018), is shown in the figure.

4.2.4 Red Giant Branch Kinematics

In order to separate the stellar populations at the level of the RGB I followed the same steps described in the previous section regards the MS. Now, I will go quickly throught them:

1. In this case, I have a lower number of stars in the RGB, therefore i could not remove the stars in the inner 50 *arcsec* from the cluster center otherwise I would ruin the statistics, therefore in this case I keep all the stars of the cluster. As visible from figure 4.14, this time the separation of the sequence is not so visible, however it is possible to see a hint of a separation of the sequence in two subsequence in the lower part of the plot.

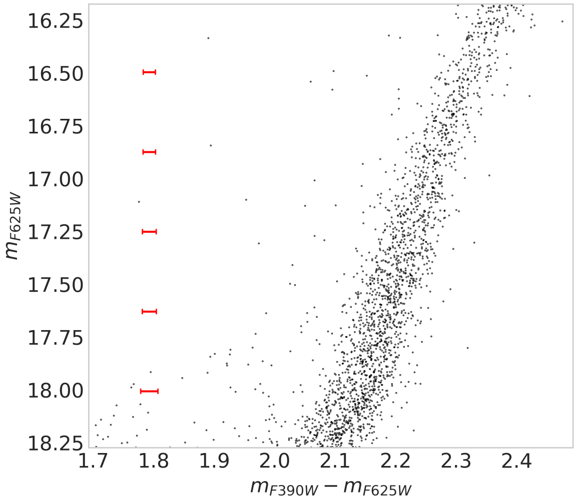

Figure 4.14: Focusing on the RGB of NGC 6266, the stars in the cluster's innermost region were not excluded due to the lower star count. The RGB displays a subtle indication of a bimodal sequence. Photometric errors, indicated in red in the plot, confirm that the broadening of the sequence has intrinsic origin.

2. Then, I proceed verticalizing the RGB. As done before, the best CMD to investigate multiple populations have colors $m_{F390W} - m_{F625W}$ and $m_{F435W} - m_{F658N}$, both plotted against m_{F625W}. Once the red and blue fiducial lines have been obtained, I used equations (4.12) and (4.13) to calculate the Δs.

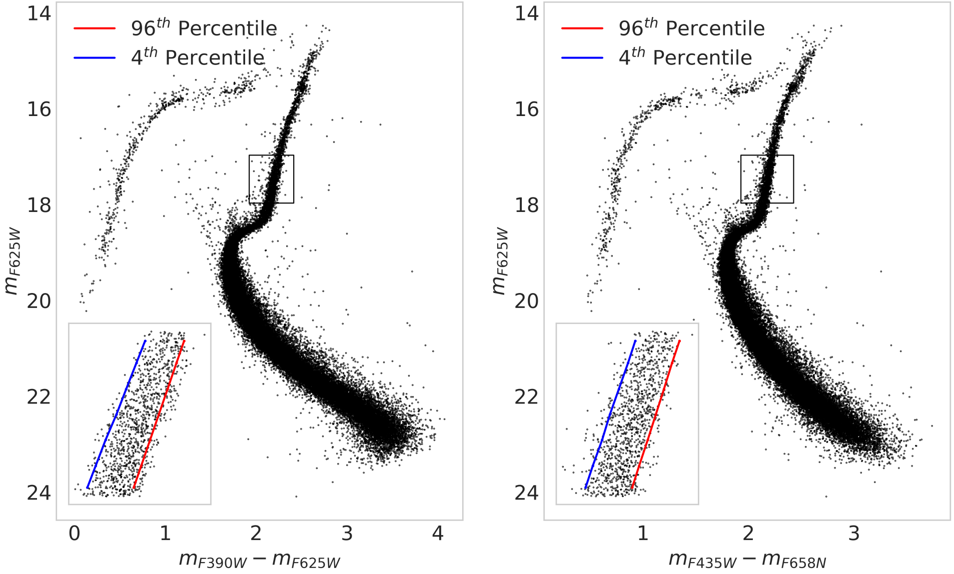

Figure 4.15: Verticalization process for both CMDs of NGC 6266. The 4$^{\text{th}}$ and 96$^{\text{th}}$ percentile are drawn, respectively, as the red and blue fiducial lines. The black box in the figure highlights the region of the CMD investigated in this study.

3. Once the Δs have been calculated, I plot both of them, one against the other to obtain the ChM for the RGB of NGC 6266, visible in figure 4.16. Also in this case, it is not possible to separate the populations from this plot, for the same resons explained before.

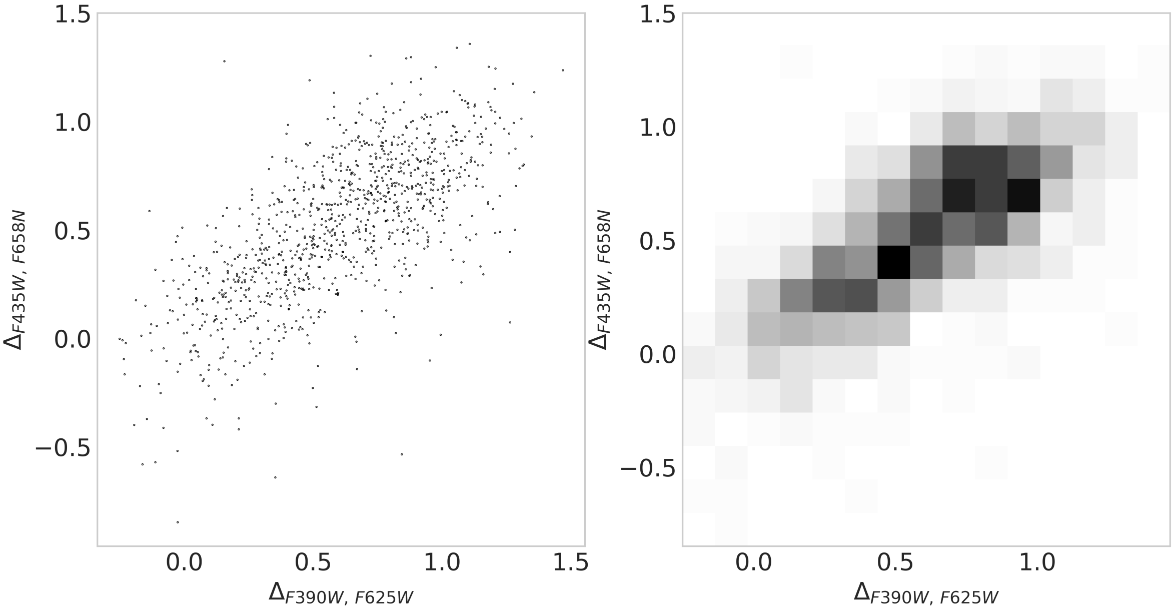

Figure 4.16: The left panel shows the ChM of NGC 6266, constructed using the two colors, $\Delta_{F390W,,F625W}$ and $\Delta_{F435W,,F658N}$. The right panel displays a two-dimensional histogram representation of the ChM. Although neither representation clearly distinguishes the populations, the two-dimensional histogram suggests a hint of bimodal distribution.

Therefore to separate them I used the histogram of $\Delta_{F390W,\,F625W}$, shown in the right pannel of figure 4.17, where I identify the two peaks, even if they are not so evident as before, as signals of the bimodal sequence of the RGB, therefore I choose the value of the valley in between them to separate the two populations as shown in the final ChM in figure 4.18.

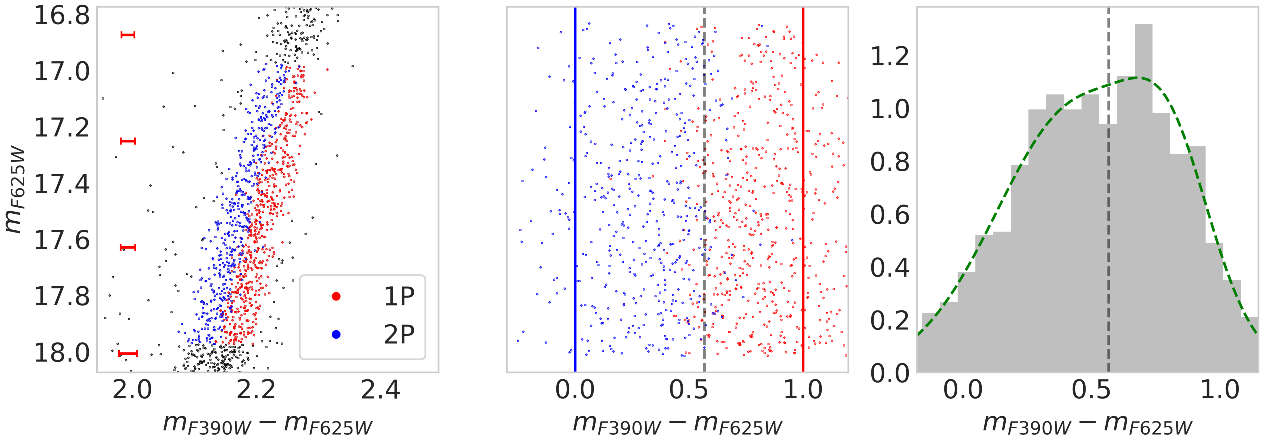

Figure 4.17: The figure shows the procedure to select 1P and 2P stars in the RGB of NGC 6266. Left panel: it shows the $m_{F390W} - m_{F625W}$ vs m_{F625W} diagram for the RGB of the cluster. The red horizontal bars represents the photometric error. Middle panel: it shows the verticalized $m_{F390W} - m_{F625W}$ vs m_{F625W} diagram for the same portion of the RGB as the left panel. Blue and red vertical lines represents respectively the $4-th$ and the $96-th$ percentile of the distribution, and highlight the boundaries of the main sequence. Right panel: it shows the $\Delta_{F390W,\,F625W}$ histogram distribution. The dashed grey vertical line is used to separate the two populations, while the dashed green line, superimposed to the histogram, represents a bimodal Gaussian distribution used to fit the data. In both, left and middle plots, red dots corresponds to 1P stars, while blue dots to 2P stars.

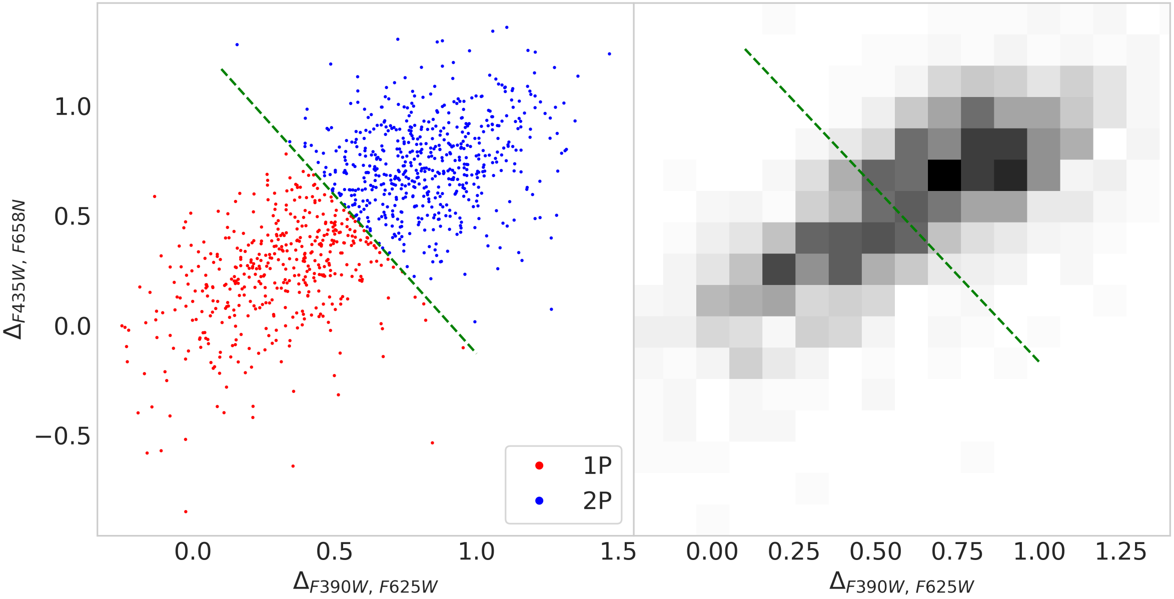

Figure 4.18: Same plots of figure 4.16 but now red and blue dots in the ChM of NGC 6266 represents respectively the first and second populations of the cluster.

Finally, examining the kinematic analysis of stars on the RGB (see Figure 4.19), we observe that these stars exhibit the same characteristics previously noted for the MS. Both radial and tangential components of motion display similar trends when analyzed as a function of distance from the cluster center. This consistency is further supported by the anisotropy coefficient, which is compatible with zero, indicating an absence of directional preference. These findings reinforce the idea that the cluster is in an isotropic state, with no significant variations in velocity dispersion across different spatial directions.

It should be noted, however, that some level of contamination between 1P and 2P stars is present in the sample, as stars from one population may have been mistakenly attributed to the other in differing proportions. This could subtly influence the observed kinematic averages and should be considered when interpreting these results.

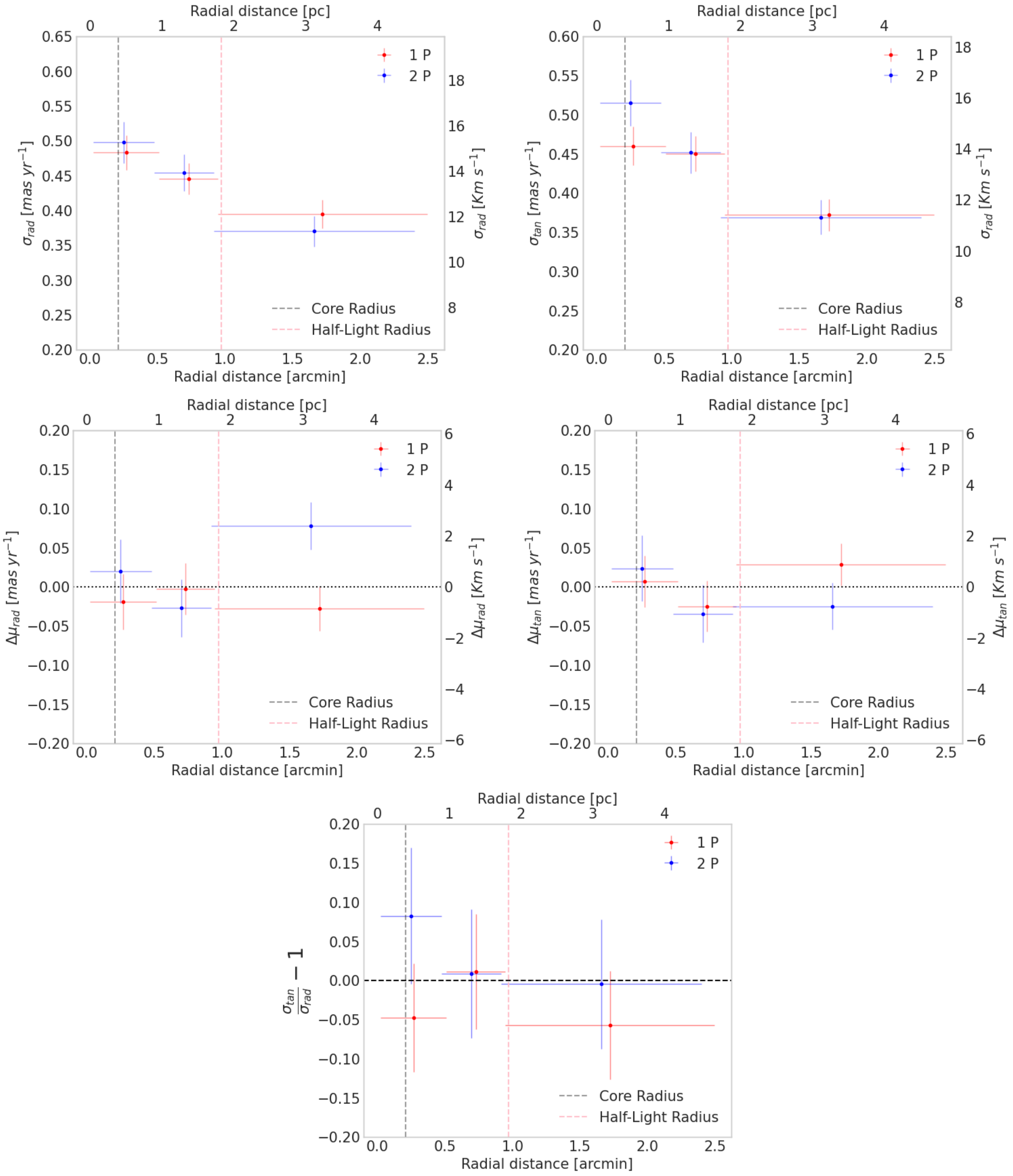

Figure 4.19: Kinematics of RGB stars of NGC 6266. The two upper plots show the average tangential and radial motions of 1P stars (red) and 2P stars (blue) as a function of the radial distance from the cluster center. The two middle plots show the velocity–dispersion profiles for the radial and tangential velocity components of the two stellar populations as a function of the radial distance from the cluster center. The bottom plot shows the anisotropy profile of the two populations. The horizontal errorbars, mark the extension of the radial bins, while the black and pink dashed lines indicate the core and the half-light radius, respectively, and their values have been taken from Baumgardt and Hilker (2018).

Chapter 5

Discussion and Conclusions

In this final chapter, I will provide a concise summary of the work conducted in this thesis, highlighting key results and discussing potential future implications.

5.1 Summary and Discussion

In this work, I analyzed the kinematics of the multiple populations within the Galactic GC NGC 6266. Specifically, I began by examining images taken with the $F390W$, $F435W$, $F625W$, and $F658N$ filters of the HST. These images were collected across two different epochs, with a time interval of roughly six years, which allowed me to derive both photometric and astrometric catalogs for this cluster using the effective PSF technique developed by Anderson et al. (2008).

The astrometric analysis first enabled me to identify cluster members and construct the CMD of NGC 6266. Then, using CMDs built from specific filter combinations, I produced the first ChM for this cluster, which allowed for the distinction of its populations both on the MS and on the RGB.

Subsequently, I developed a MCMC algorithm that enabled me to infer and analyze the kinematics of these populations in the plane of the sky. The main results of this analysis are summarized as follows:

- The ChMs obtained for both the MS and RGB do not fully separate the populations of this cluster. This limitation arises because the images were collected before the discovery that CMDs constructed with specific UV filters could effectively distinguish stellar populations. Thus, the available filters were not optimal for this purpose. Nonetheless, I was able to distinguish the two extreme populations within NGC 6266.
- No kinematic differences were observed among the MS stars in either the radial or tangential components of motion within a region extending 2.5 arcminutes from the cluster center. The anisotropy plot indicates that the motion of both populations is entirely isotropic in this region.
- For the RGB, no significant kinematic differences were detected between the populations within 2.5 arcminutes from the cluster center. Here, too, the anisotropy plot confirms an entirely isotropic motion.

The final conclusion of this work is that no kinematic differences are present among the multiple populations of NGC 6266 within a region of 2.5 arcminutes from the cluster center.

This result aligns with the conclusions of Libralato et al. (2022), who categorized GCs into three types based on their dynamical ages, defined as the ratio between the cluster's age and its **half-mass relaxation time**, t_{rh}. They proposed the following categories:

1. **Dynamically old** clusters, defined by $\frac{\text{Age}}{t_{rh}} \geq 10$. These clusters are typically isotropic in their central regions, reaching isotropy already at the half-light radius.

2. **Intermediate-age** clusters, for which $7 \leq \frac{\text{Age}}{t_{rh}} \leq 10$. These clusters represent a transitional category, where kinematic differences between populations may or may not be observed.
3. **Dynamically young** clusters, characterized by $\frac{\text{Age}}{t_{rh}} \leq 7$. These systems display radial anisotropic motion among the stars in their populations.

Although observationally based, this classification is consistent with theoretical expectations set by Vesperini et al. (2013) and is further supported by subsequent studies such as those by Milone et al. (2018b); Cordoni et al. (2020, 2024).
For NGC 6266, with an age of 11.78 Gyr and a half-mass relaxation time of $t_{rh} = 10^{9.13}$ yr (Baumgardt and Hilker, 2018), the resulting dynamical age is 8.73. Based on the classification proposed by Libralato et al. (2022), this places NGC 6266 among intermediate-age GCs. This categorization may provide an explanation for the isotropic behavior observed in the cluster's two populations, as it suggests that no kinematic differences are expected to manifest in the innermost regions of the cluster.

The physical mechanism behind the erasure of kinematic signatures among stars—implied when discussing a cluster's dynamical age—is **two-body relaxation**. This process describes how individual stars in a dense environment like a GC gradually alter their trajectories due to gravitational interactions with other stars. In GCs, these interactions manifest as a sequence of minor, distant fly-bys that, over time, accumulate to significantly alter a star's original motion. The term relaxation refers to the way each star settles into a new orbit as these small perturbations accumulate. Additionally, two-body relaxation drives the cluster towards energy equipartition and segregation, causing heavier, slower stars to move inward while lighter, faster stars tend toward the outer regions.

However, it is important to note that, based on the studies conducted so far in this field and the results of this work, we cannot conclude that two-body relaxation is the sole mechanism driving the dynamical evolution of the cluster. There are still many uncertainties surrounding the mechanisms of cluster formation, which remain not fully understood.

5.2 Future Investigations

The results of this thesis can be further enhanced through new observations that improve the precision of the proper motions by adding an additional epoch of data. Furthermore, using appropriate HST filters could facilitate better separation of the multiple populations.

Another approach to enhance this work involves exploring the outer regions of the cluster with instruments that have a larger FoV, such as Gaia. While this may result in a slight loss of precision in proper motion detection, it would allow for observations at a much larger radial distance. This could enable us to investigate regions where two-body relaxation has not completely erased any kinematic differences among the two populations of NGC 6266.

Bibliography

Anderson, J. and King, I. R. (2000). Toward high-precision astrometry with wfpc2. i. deriving an accurate point-spread function. *Publications of the Astronomical Society of the Pacific*, 112(776):1360.

Anderson, J., King, I. R., Richer, H. B., Fahlman, G. G., Hansen, B. M., Hurley, J., Kalirai, J. S., Rich, R. M., and Stetson, P. B. (2008). Deep advanced camera for surveys imaging in the globular cluster ngc 6397: reduction methods. *The Astronomical Journal*, 135(6):2114.

Bastian, N., Lamers, H., de Mink, S., Longmore, S., Goodwin, S., and Gieles, M. (2013). Early disc accretion as the origin of abundance anomalies in globular clusters. *Monthly Notices of the Royal Astronomical Society*, 436(3):2398–2411.

Baumgardt, H. and Hilker, M. (2018). A catalogue of masses, structural parameters, and velocity dispersion profiles of 112 milky way globular clusters. *Monthly Notices of the Royal Astronomical Society*, 478(2):1520–1557.

Bekki, K. and Tsujimoto, T. (2016). Formation of anomalous globular clusters with metallicity spreads: a unified picture. *Astrophysical Journal*, 831(1):70.

Bocquet, S. and Carter, F. W. (2016). pygtc: beautiful parameter covariance plots (aka. giant triangle confusograms). *The Journal of Open Source Software*, 1(6).

Bonnarel, F., Fernique, P., Bienaymé, O., Egret, D., Genova, F., Louys, M., Ochsenbein, F., Wenger, M., and Bartlett, J. G. (2000). The aladin interactive sky atlas-a reference tool for identification of astronomical sources. *Astronomy and Astrophysics Supplement Series*, 143(1):33–40.

Carretta, E., Bragaglia, A., Gratton, R., and Lucatello, S. (2009). Na-o anticorrelation and hb-viii. proton-capture elements and metallicities in 17 globular clusters from uves spectra. *Astronomy & Astrophysics*, 505(1):139–155.

Cordoni, G., Casagrande, L., Milone, A., Dondoglio, E., Mastrobuono-Battisti, A., Jang, S., Marino, A., Lagioia, E., Legnardi, M. V., Ziliotto, T., et al. (2024). Internal dynamics of multiple populations in 28 galactic globular clusters: A wide-field study with gaia and the hubble space telescope. *arXiv preprint arXiv:2409.02330*.

Cordoni, G Cordoni, G., Milone, A., Mastrobuono-Battisti, A., Marino, A., Lagioia, E., Tailo, M., Baumgardt, H., and Hilker, M. (2020). Three-component kinematics of multiple stellar populations in globular clusters with gaia and vlt. *Astrophysical Journal*, 889(1):18.

Decressin, T., Meynet, G., Charbonnel, C., Prantzos, N., and Ekström, S. (2007). Fast rotating massive stars and the origin of the abundance patterns in galactic globular clusters. *Astronomy & Astrophysics*, 464(3):1029–1044.

Dotter, A., Sarajedini, A., Anderson, J., Aparicio, A., Bedin, L. R., Chaboyer, B., Majewski, S., Marín-Franch, A., Milone, A., Paust, N., et al. (2009). The acs survey of galactic globular clusters. ix. horizontal branch morphology and the second parameter phenomenon. *The Astrophysical Journal*, 708(1):698.

Draine, B. T. (2003). Interstellar dust grains. *Annual Review of Astronomy and Astrophysics*, 41(1):241–289.

Foreman-Mackey, D., Hogg, D. W., Lang, D., and Goodman, J. (2013). emcee: the mcmc hammer. *Publications of the Astronomical Society of the Pacific*, 125(925):306.

GaiaCollaboration (2018). Gaia data release 2 summary of the contents and survey properties. *Astronomy & Astrophysics*, 616(1).

Gieles, M., Charbonnel, C., Krause, M. G., Hénault-Brunet, V., Agertz, O., Lamers, H. J., Bastian, N., Gualandris, A., Zocchi, A., and Petts, J. A. (2018). Concurrent formation of supermassive stars and globular clusters: implications for early self-enrichment. *Monthly Notices of the Royal Astronomical Society*, 478(2):2461–2479.

Häberle, M., Neumayer, N., Seth, A., Bellini, A., Libralato, M., Baumgardt, H., Whitaker, M., Dumont, A., Alfaro-Cuello, M., Anderson, J., et al. (2024). Fast-moving stars around an intermediate-mass black hole in ω centauri. *Nature*, 631(8020):285–288.

Harris, C. R., Millman, K. J., van der Walt, S. J., Gommers, R., Virtanen, P., Cournapeau, D., Wieser, E., Taylor, J., Berg, S., Smith, N. J., Kern, R., Picus, M., Hoyer, S., van Kerkwijk, M. H., Brett, M., Haldane, A., del Río, J. F., Wiebe, M., Peterson, P., Gérard-Marchant, P., Sheppard, K., Reddy, T., Weckesser, W., Abbasi, H., Gohlke, C., and Oliphant, T. E. (2020). Array programming with NumPy. *Nature*, 585(7825):357–362.

Hunter, J. D. (2007). Matplotlib: A 2d graphics environment. *Computing in Science & Engineering*, 9(3):90–95.

Ibata, R. A., Gilmore, G., and Irwin, M. (1994). A dwarf satellite galaxy in sagittarius. *Nature*, 370(6486):194–196.

Johnson, H. L. (1955). A photometric system. *Annales d'Astrophysique, Vol. 18, p. 292*, 18:292.

Krause, M., Charbonnel, C., Decressin, T., Meynet, G., and Prantzos, N. (2013). Superbubble dynamics in globular cluster infancy-ii. consequences for secondary star formation in the context of self-enrichment via fast-rotating massive stars. *Astronomy & Astrophysics*, 552:A121.

Lagioia, E. P., Milone, A. P., Marino, A. F., Cordoni, G., and Tailo, M. (2019). The role of cluster mass in the multiple populations of galactic and extragalactic globular clusters. *The Astronomical Journal*, 158(5):202.

Legnardi, M., Milone, A., Cordoni, G., Lagioia, E., Dondoglio, E., Marino, A., Jang, S., Mohandasan, A., and Ziliotto, T. (2023). Differential reddening in the direction of 56 galactic globular clusters. *Monthly Notices of the Royal Astronomical Society*, 522(1):367–380.

Libralato, M., Bellini, A., Vesperini, E., Piotto, G., Milone, A. P., van der Marel, R. P., Anderson, J., Aparicio, A., Barbuy, B., Bedin, L. R., et al. (2022). The hubble space telescope uv legacy survey of galactic globular clusters. xxiii. proper-motion catalogs and internal kinematics. *The Astrophysical Journal*, 934(2):150.

Mackey, A., Da Costa, G., Ferguson, A., and Yong, D. (2012). A vlt/flames study of the peculiar intermediate-age large magellanic cloud star cluster ngc 1846. i. kinematics. *The Astrophysical Journal*, 762(1):65.

Marino, A., Milone, A., Renzini, A., D'Antona, F., Anderson, J., Bedin, L., Bellini, A., Cordoni, G., Lagioia, E., Piotto, G., et al. (2019). The hubble space telescope uv legacy survey of galactic globular clusters–xix. a chemical tagging of the multiple stellar populations over the chromosome maps. *Monthly Notices of the Royal Astronomical Society*, 487(3):3815–3844.

Marino, A., Milone, A., Renzini, A., Yong, D., Asplund, M., Da Costa, G., Jerjen, H., Cordoni, G., Carlos, M., Dondoglio, E., et al. (2021). Spectroscopy and photometry of the least massive type ii globular clusters: Ngc 1261 and ngc 6934. *The Astrophysical Journal*, 923(1):22.

Mehta, V., Milone, A., Casagrande, L., Marino, A., Legnardi, M., Cordoni, G., Dondoglio, E., Jang, S., Ziliotto, T., Barbieri, M., et al. (2024). Spectro-photometry and radial distribution of multiple stellar populations in globular clusters from gaia xp spectra. *arXiv preprint arXiv:2406.02755*.

Metropolis, N., Rosenbluth, A. W., Rosenbluth, M. N., Teller, A. H., and Teller, E. (1953). Equation of state calculations by fast computing machines. *The journal of chemical physics*, 21(6):1087–1092.

Milone, A. (2015). Helium and multiple populations in the massive globular cluster ngc 6266 (m 62). *Monthly Notices of the Royal Astronomical Society*, 446(2):1672–1684.

Milone, A., Marino, A., Bedin, L., Anderson, J., Apai, D., Bellini, A., Dieball, A., Salaris, M., Libralato, M., Nardiello, D., et al. (2019). The hst large programme on ngc 6752–ii. multiple populations at the bottom of the main sequence probed in nir. *Monthly Notices of the Royal Astronomical Society*, 484(3):4046–4053.

Milone, A., Marino, A., Piotto, G., Renzini, A., Bedin, L., Anderson, J., Cassisi, S., D'Antona, F., Bellini, A., Jerjen, H., et al. (2015). The hubble space telescope uv legacy survey of galactic globular clusters. iii. a quintuple stellar population in ngc 2808. *The Astrophysical Journal*, 808(1):51.

Milone, A., Marino, A., Renzini, A., D'Antona, F., Anderson, J., Barbuy, B., Bedin, L., Bellini, A., Brown, T., Cassisi, S., et al. (2018a). The hubble space telescope uv legacy survey of galactic globular clusters–xvi. the helium abundance of multiple populations. *Monthly Notices of the Royal Astronomical Society*, 481(4):5098–5122.

Milone, A., Piotto, G., Bedin, L., Aparicio, A., Anderson, J., Sarajedini, A., Marino, A., Moretti, A., Davies, M. B., Chaboyer, B., et al. (2012). The acs survey of galactic globular clusters-xii. photometric binaries along the main sequence. *Astronomy & Astrophysics*, 540:A16.

Milone, A., Piotto, G., Bedin, L., King, I., Anderson, J., Marino, A., Bellini, A., Gratton, R., Renzini, A., Stetson, P., et al. (2011). Multiple stellar populations in 47 tucanae. *The Astrophysical Journal*, 744(1):58.

Milone, A. P., Marino, A. F., Mastrobuono-Battisti, A., and Lagioia, E. (2018b). Gaia unveils the kinematics of multiple stellar populations in 47 tucanae. *Monthly Notices of the Royal Astronomical Society*, 479(4):5005–5011.

Milone, A. P., Piotto, G., Renzini, A., Marino, A. F., Bedin, L., Vesperini, E., D'Antona, F., Nardiello, D., Anderson, J., King, I., et al. (2017). The hubble space telescope uv legacy survey of galactic globular clusters–ix. the atlas of multiple stellar populations. *Monthly Notices of the Royal Astronomical Society*, 464(3):3636–3656.

Norris, J., Cottrell, P., Freeman, K., and Da Costa, G. (1981). The abundance spread in the giants of ngc 6752. *Astrophysical Journal, Part 1, vol. 244, Feb. 15, 1981, p. 205-220.*, 244:205–220.

Norris, J. and Freeman, K. (1982). The anticorrelation of carbon and nitrogen on the horizontal branch of 47 tucanae. *Astrophysical Journal, Part 1, vol. 254, Mar. 1, 1982, p. 143-148.*, 254:143–148.

Noyola, E., Gebhardt, K., and Bergmann, M. (2008). Gemini and hubble space telescope evidence for an intermediate-mass black hole in ω centauri. *The Astrophysical Journal*, 676(2):1008.

pandas development team, T. (2020). pandas-dev/pandas: Pandas.

Pedregosa, F., Varoquaux, G., Gramfort, A., Michel, V., Thirion, B., Grisel, O., Blondel, M., Prettenhofer, P., Weiss, R., Dubourg, V., Vanderplas, J., Passos, A., Cournapeau, D., Brucher, M., Perrot, M., and Duchesnay, É. (2011). Scikit-learn: Machine learning in python. *Journal of Machine Learning Research*, 12:2825–2830.

Renzini, A. (2013). Rethinking globular cluster formation. *arXiv preprint arXiv:1302.0329*.

Renzini, A. and Buzzoni, A. (1986). Global properties of stellar populations and the spectral evolution of galaxies. In *Spectral Evolution of Galaxies: Proceedings of the Fourth Workshop of the Advanced*

School of Astronomy of the "Ettore Majorana" Centre for Scientific Culture, Erice, Italy, March 12–22, 1985, pages 195–235. Springer.

Scalco, M., Gerasimov, R., Bedin, L. R., Vesperini, E., Nardiello, D., Salaris, M., Burgasser, A., Anderson, J., Libralato, M., Bellini, A., et al. (2024). The hst large programme on ngc 6752-v. differences in luminosity and mass function among stellar populations. *Astronomische Nachrichten*, page e20240018.

Sivia, D. and Skilling, J. (2006). *Data analysis: a Bayesian tutorial*. OUP Oxford.

Van der Marel, R. P. and Anderson, J. (2010). New limits on an intermediate-mass black hole in omega centauri. ii. dynamical models. *The Astrophysical Journal*, 710(2):1063.

Ventura, P., D'Antona, F., Mazzitelli, I., and Gratton, R. (2001). Predictions for self-pollution in globular cluster stars. *Astrophysical Journal*, 550(1):L65.

Verma, K., Raodeo, K., Basu, S., Silva Aguirre, V., Mazumdar, A., Mosumgaard, J. R., Lund, M. N., and Ranadive, P. (2019). Helium abundance in a sample of cool stars: measurements from asteroseismology. *Monthly Notices of the Royal Astronomical Society*, 483(4):4678–4694.

Vesperini, E., Hong, J., Giersz, M., and Hypki, A. (2021). Dynamical evolution of multiple-population globular clusters. *Monthly Notices of the Royal Astronomical Society*, 502(3):4290–4304.

Vesperini, E., McMillan, S. L., D'Antona, F., and D'Ercole, A. (2013). Dynamical evolution and spatial mixing of multiple population globular clusters. *Monthly Notices of the Royal Astronomical Society*, 429(3):1913–1921.

Vesperini, E., Varri, A. L., McMillan, S. L., and Zepf, S. E. (2014). Kinematical fingerprints of star cluster early dynamical evolution. *Monthly Notices of the Royal Astronomical Society*, 443(1):L79–L83.

Virtanen, P., Gommers, R., Oliphant, T. E., Haberland, M., Reddy, T., Cournapeau, D., Burovski, E., Peterson, P., Weckesser, W., Bright, J., van der Walt, S. J., Brett, M., Wilson, J., Millman, K. J., Mayorov, N., Nelson, A. R. J., Jones, E., Kern, R., Larson, E., Carey, C. J., Polat, İ., Feng, Y., Moore, E. W., VanderPlas, J., Laxalde, D., Perktold, J., Cimrman, R., Henriksen, I., Quintero, E. A., Harris, C. R., Archibald, A. M., Ribeiro, A. H., Pedregosa, F., van Mulbregt, P., and SciPy 1.0 Contributors (2020). SciPy 1.0: Fundamental Algorithms for Scientific Computing in Python. *Nature Methods*, 17:261–272.

Walker, M. G., Mateo, M., Olszewski, E. W., Bernstein, R., Wang, X., and Woodroofe, M. (2006). Internal kinematics of the fornax dwarf spheroidal galaxy. *The Astronomical Journal*, 131(4):2114.

Wes McKinney (2010). Data Structures for Statistical Computing in Python. In Stéfan van der Walt and Jarrod Millman, editors, *Proceedings of the 9th Python in Science Conference*, pages 56 – 61.

Zennaro, M., Milone, A., Marino, A., Cordoni, G., Lagioia, E., and Tailo, M. (2019). Four stellar populations and extreme helium variation in the massive outer-halo globular cluster ngc 2419. *Monthly Notices of the Royal Astronomical Society*, 487(3):3239–3251.

Ziliotto, T., Milone, A., Marino, A. F., Dotter, A. L., Renzini, A., Vesperini, E., Karakas, A., Cordoni, G., Dondoglio, E., Legnardi, M. V., et al. (2023). Multiple stellar populations in metal-poor globular clusters with jwst: A nircam view of m92. *The Astrophysical Journal*, 953(1):62.